



**HAL**  
open science

## A 9 myr cycle in Cenozoic $\delta^{13}\text{C}$ record and long-term orbital eccentricity modulation: Is there a link?

Slah Boulila, Bruno Galbrun, Jacques Laskar, Heiko Pälike

### ► To cite this version:

Slah Boulila, Bruno Galbrun, Jacques Laskar, Heiko Pälike. A 9 myr cycle in Cenozoic  $\delta^{13}\text{C}$  record and long-term orbital eccentricity modulation: Is there a link?. *Earth and Planetary Science Letters*, 2012, 317, pp.273-281. 10.1016/j.epsl.2011.11.017. hal-00657907

**HAL Id: hal-00657907**

**<https://hal.science/hal-00657907v1>**

Submitted on 10 Jan 2012

**HAL** is a multi-disciplinary open access archive for the deposit and dissemination of scientific research documents, whether they are published or not. The documents may come from teaching and research institutions in France or abroad, or from public or private research centers.

L'archive ouverte pluridisciplinaire **HAL**, est destinée au dépôt et à la diffusion de documents scientifiques de niveau recherche, publiés ou non, émanant des établissements d'enseignement et de recherche français ou étrangers, des laboratoires publics ou privés.

3  
4 **A ~9 myr cycle in Cenozoic  $\delta^{13}\text{C}$  record and long-term orbital eccentricity**  
5 **modulation: Is there a link?**

6  
7  
8 Slah Boulila <sup>a,b,\*</sup>, Bruno Galbrun <sup>a</sup>, Jacques Laskar <sup>b</sup>, and Heiko Pälike <sup>c</sup>

9  
10 <sup>a</sup> Université Paris VI, CNRS - UMR 7193 IStEP 'Institut des Sciences de la Terre-Paris',  
11 case 117, 4, place Jussieu, 75252 Paris cedex 05, France

12 <sup>b</sup> ASD, IMCCE-CNRS UMR8028, Observatoire de Paris, UPMC,  
13 77 avenue Denfert-Rochereau, 75014 Paris, France

14 <sup>c</sup> National Oceanography Centre, Southampton, School of Ocean and Earth Science,  
15 European Way, Southampton SO14 3ZH, UK

16  
17  
18 \* Corresponding author. Tel.: +33 144274163; Fax: +33 144273831

19  
20 Email addresses: slah.boulila@upmc.fr (S. Boulila), bruno.galbrun@upmc.fr (B. Galbrun),  
21 laskar@imcce.fr (J. Laskar), H.Palike@soton.ac.uk (H. Pälike).

22  
23  
24 **Abstract**

25  
26 The ~65-my-long Cenozoic carbon isotope record ( $\delta^{13}\text{C}$ ) of [Zachos et al. \(2001,](#)  
27 [2008\)](#) documents a strong long-term cycle with a mean pseudoperiodicity close to ~9 myr.

28 This cyclicity modulates the ~2.4 myr eccentricity cycle amplitude, hinting at a possible link  
29 between long-term astronomical and geological variations. Some phase shifts between ~9-  
30 myr  $\delta^{13}\text{C}$  and astronomical cycles suggest that additional processes (e.g., tectonics)  
31 contribute to these long-term carbon-cycle variations.

32

33 The strong response of  $\delta^{13}\text{C}$  to long-term eccentricity periods (~9 myr, ~2.4 myr, ~400  
34 kyr) supports the hypothesis that the long time-residence of carbon in the oceans amplifies  
35 lower frequency or dampens higher frequency orbital variations. Additionally, the strong  
36 expression of low-amplitude ~9 myr eccentricity cycle in the  $\delta^{13}\text{C}$  record could be explained  
37 by energy-transfer process from higher to lower frequency cycles, and all eccentricity  
38 components modulate the carrier climatic precession cycles.

39

40 Finally, the Paleocene-Eocene Thermal Maximum (PETM, 55.9 Ma) event, which  
41 corresponds to a pronounced  $\delta^{13}\text{C}$  negative excursion, is situated within a strong decrease in  
42 the most prominent ~9 myr  $\delta^{13}\text{C}$  cycle, hinting at a link between accelerated rates in  $\delta^{13}\text{C}$   
43 variations and the PETM. This specific ~9 myr  $\delta^{13}\text{C}$  cycle seems to be amplified by non-  
44 orbital mechanisms in atmosphere-continent-ocean system, such as previously suggested  
45 methane release from gas hydrate and volcanism.

46

47

48 **Keywords:** Cenozoic deep-sea  $\delta^{13}\text{C}$  records, multi-millionyear cyclicity, ~9 myr cyclicity,  
49 astronomical driving force, eccentricity.

50

51

52 **1. Introduction**

53

54 It has been widely demonstrated that Earth's orbital parameters (climatic precession,  
55 obliquity, eccentricity) control paleoclimate changes induced by variations in solar radiation  
56 intensity received by our planet (Hays et al., 1976; Imbrie et al., 1984). Research has  
57 documented the Earth's orbital parameters in the geologic record over broad time scales,  
58 from millennial to million year time scales. Today, there is a broad consensus that insolation  
59 forcing from the Earth's orbital parameters is a major external driver of changes in  
60 atmospheric, continental, and oceanic conditions across all latitudes. Accordingly, recent  
61 research has now turned to explain extreme short-lived climate events (e.g., Lourens et al.,  
62 2005), ice-sheet formation and carbon reservoir cycling (e.g., Pälike et al., 2006a), biotic  
63 extinctions (van Dam et al., 2006), and other poorly understood phenomena. Reciprocally,  
64 geophysical processes, such as a post-glacial rebound (Laskar et al., 1993; Mitrovica et al.,  
65 1997) and mantle convection (Forte & Mitrovica, 1997), could have influenced secular  
66 variations in the dynamic ellipticity of the Earth, which consequently influence the  
67 astronomical precession constant value (e.g., Berger et al., 1992).

68 In this study, we focus on very long-term periodic variations in the carbon isotope  
69 record ( $\delta^{13}\text{C}$ ) of Cenozoic deep-sea sediments by which we suggest a possible link with long-  
70 term astronomical modulation cycle. Numerous Cenozoic and Mesozoic studies have  
71 interpreted these long-term carbon cycle variations as trends, most of them suggesting a  
72 tectonic origin (e.g., Zachos et al., 2001; Leckie et al., 2002; Li et al., 2009). Through a  
73 comparison between long-term  $\delta^{13}\text{C}$  cycle and orbital eccentricity modulation cycle, we  
74 suggest another alternative, i.e., orbital driving force.

75 Additionally, our results concur with and build on previous studies pointing to the long  
76 residence-time of carbon in oceans amplified by longer orbital periods (Pälike et al., 2006a).  
77 At the same time, we do not rule out possible interactions between tectono-oceanic and  
78 climatic variations (e.g., Raymo and Ruddiman, 1992; Lagabriele et al., 2009) in carbon  
79 recycling, triggered or retroacted by the astronomical driving force.

80

## 81 **2. Cenozoic carbon isotope record ( $\delta^{13}\text{C}$ )**

82

83 Building on ocean drilling during the last three decades, ~65-myr-long Cenozoic  
84 carbon and oxygen records ( $\delta^{13}\text{C}$  and  $\delta^{18}\text{O}$ ) were compiled from benthic foraminifera isotope  
85 data from more than 40 deep-sea cores of the Deep Sea Drilling Project (DSDP) and Ocean  
86 Drilling Program (ODP) (Zachos et al., 2001, 2008, Fig. S1, and Cramer et al., 2009). Today,  
87 these long records serve as a basic reference for numerous Cenozoic paleoclimate studies  
88 that address rhythms, trends and events in Earth's changing climate (Zachos et al., 2001).  
89 The compiled records of Zachos et al.'s (2008) compilation exhibit variable resolution, which  
90 is comprised between less than ~1 kyr and ~8 kyr for the last ~34 Ma, and could reach 40 kyr  
91 for the last 35 to 65 Ma interval (Zachos et al., 2008). This resolution of the stacked data is  
92 however sufficient for time-series analysis of low-frequency (multi-millionyear) variations. In  
93 this study, we examine the behavior of long-period cycles in the  $\delta^{13}\text{C}$  record (Fig. 1), and in  
94 particular, we suggest a possible link with long-term eccentricity cycling throughout the  
95 Cenozoic (Section 3).

96 The ~65-myr-long Cenozoic carbon record shows evidence of ~9-myr cycles that we  
97 denote as Cb1 to Cb8 (Fig. 1). Zachos et al.'s (2001) studies were focused on oxygen  
98 isotope evolution to interpret temperature and glacial trends and short-lived events such as  
99 the Paleocene-Eocene Thermal Maximum (PETM), Oi-1, Mi-1 glaciation events, etc. The Oi-  
100 1 and Mi-1 events delimit the Cb4 cycle, which roughly spans the Oligocene Epoch. This  
101 cycle was studied in detail by Pälike et al. (2006a) at a ~4-kyr sampling resolution (Fig. 2a),  
102 who demonstrated the strong expression of the ~400-kyr cycles in the carbon isotope signal.  
103 Filtering and modulation analysis studies were focused mainly on the ~100-kyr eccentricity  
104 and 41-kyr obliquity bands to recover the important ~1.2 and ~2.4-myr astronomical

105 modulations. Modulation behavior of the lower frequency ~400-kyr and ~2.4-myr eccentricity  
106 cycles (Section 3.2) were not examined.

107 In fact, because the Oligocene interval is only 11.9-myr long (from 22 to 33.9 Ma),  
108 [Pälike et al. \(2006a\)](#) did not consider Cb4 to be a true cycle (Section 3). Instead, they  
109 subdivided the interval into 4 phases, which they interpreted as long-term trends, through  
110 comparison with the oxygen isotope record (see their Figure 1). Here, we show that this  
111 cycle, Cb4, contains four ~2.4-myr cycles easily correlatable to their analogs in astronomical  
112 solutions ([Laskar et al., 2004](#), and [Laskar et al., 2011a](#)). The ~2.4-myr term acts to modulate  
113 the ~400-kyr cycles, while the 'Cb4' modulates the 2.4-myr cycles ([Figs. 1 and 2a](#), Section  
114 3.2).

115

### 116 **3. Methods and results**

117

#### 118 **3.1. Spectral analysis**

119

##### 120 **3.1.1. Spectral analysis of $\delta^{13}\text{C}$ data**

121

122 Spectral analysis of the raw  $\delta^{13}\text{C}$  record of [Zachos et al.'s \(2008\)](#) compilation shows  
123 two dominant peaks centered on periods of 27 and 8.4 myr ([Fig. 3a](#)). Similar results are  
124 obtained when we consider the same interval (i.e., Cenozoic) in [Cramer et al.'s \(2009\)](#)  $\delta^{13}\text{C}$   
125 compilation ([Fig. 3b](#)). The 8.4 myr cyclicity is prominent in the  $\delta^{13}\text{C}$  records and represent the  
126 cycles denoted Cb1 to Cb8 ([Fig. 1](#)). Its pseudo-period could vary from ~7.5 myr (Cb2) to ~11  
127 myr (Cb3). However, the 27 myr peak is not evident in  $\delta^{13}\text{C}$  time series, but it may  
128 correspond to the two cycles delimited by the minima of Cb1, Cb4 and Cb7 ([Figs. S1 and](#)  
129 [S2](#)). These very long-term  $\delta^{13}\text{C}$  oscillations have a significant effect on spectral results. When  
130 we subtract them, other peaks at higher frequency band are strengthened, but still with low

131 power because of the high-power  $\sim 9$  myr peak (Fig. S2). To highlight low- and high-  
132 frequency bands, we display the raw  $\delta^{13}\text{C}$  spectrum, associated with the robust noise, on a  
133 logarithmic scale (Figs. 3c,d). Zachos et al.'s (2008) compilation (Fig. 3c) shows several  
134 spectral peaks around the 400 kyr band, but none of them matches the astronomically  
135 predicted and well defined 405 kyr eccentricity term; one peak centered on the period of 1.2  
136 myr, likely related to long-term obliquity modulation cycle; and two other peaks at 1.9 and 2.5  
137 myr periods, may represent the 2.4 myr orbital eccentricity term. Cramer et al.'s (2009)  
138 compilation (Fig. 3d) shows also several peaks around the 400 kyr band, only one peak (404  
139 kyr, see also Fig. S2) may correspond to the 405 kyr eccentricity period. This mismatch  
140 between  $\delta^{13}\text{C}$  and astronomical periodicities may be due to the sampling rates in these  
141 stacked  $\delta^{13}\text{C}$  data (see Section 3.2). Differences in spectral analysis results between the two  
142  $\delta^{13}\text{C}$  compilations (i.e., Zachos et al., 2008; Cramer et al., 2009) concur with this hypothesis  
143 of the sampling-rate effect. Nevertheless, the multi-myrr  $\delta^{13}\text{C}$  cycles are robust and persistent  
144 in both compilations (Figs. 3a,b). Particularly, the  $\sim 9$  myr cycles are well detected by lowpass  
145 and bandpass filtering of the two  $\delta^{13}\text{C}$  time series (Fig. 1). The 405 kyr and 2.4 myr  $\delta^{13}\text{C}$   
146 cyclicities are documented with confidence in the single ODP site 1218 (Fig. 2a, Pälike et al.,  
147 2006a), which respectively reflect 'g2-g5' and 'g4-g3' eccentricity terms (where g2, g3, g4,  
148 and g5 are respectively related to the precession of the perihelions of Venus, the Earth,  
149 Mars, and Jupiter, Fig. 4). However, neither 8.4 nor 27-myrr cycles is evident in the Earth's  
150 orbital variations (e.g., Laskar et al., 2004). To determine if these long-term cycles have an  
151 astronomical origin, we tested their presence in two astronomical models, La2004 and the  
152 most recent and constrained La2010d (Laskar et al., 2004; Laskar et al., 2011a).

153

### 154 3.1.2. Spectral analysis of the orbital eccentricity variations

155

156           The objective of this section is to test if there are small (low amplitudes) low-  
157 frequency (periods longer than  $\sim 2.4$  myr) cyclicities in the raw eccentricity time series. Thus,  
158 we applied spectral analysis (Figs. 4a,b) to the La2004 and La2010d orbital eccentricity for  
159 the last 67 Ma (time interval equivalent to that in  $\delta^{13}\text{C}$  records).

160

161           The La2004 model was demonstrated as precise for the last 40 Ma (Laskar et al.,  
162 2004). The La2010d is the most constrained version of the La2010 astronomical model that  
163 extends the precision to the last 50 Ma (Laskar et al., 2011a,b). The main difference between  
164 La2004 and La2010 models is that the La2004 initial conditions are adjusted to the JPL  
165 numerical ephemeris DE406 (Standish, 1998) over  $-5000$  yr to  $+1000$  yr from the present  
166 date, while La2010 is fitted to the most precise planetary ephemeris INPOP06 and INPOP08  
167 (Fienga et al., 2008, 2009). In particular, La2010d version is adjusted to the INPOP06 over  
168 the last 1 Ma that includes the five major asteroids, Ceres, Vesta, Pallas, Iris, and Bamberga.  
169 La2010a, La2010b and La2010c are fitted to the INPOP08 over only 580 kyr for La2010a  
170 and La2010b, and over 1 myr for La2010c. However, the latter does not include the five  
171 major asteroids, Ceres, Vesta, Pallas, Iris, and Bamberga. Certain orbits of these asteroids  
172 underwent a strong chaotic behavior, and consequently their motion will be unpredictable  
173 over 400 kyr, which in turn influences the Earth's orbital eccentricity calculation (for detail see  
174 Laskar et al., 2010b). Thus, the La2010d version is considered as the most constrained  
175 version in the La2010 model (Laskar et al., 2010b).

176

177           Frequency decomposition in harmonic analysis of both La2004 and La2010d raw  
178 eccentricity are very similar (Figs. 4a,b). However, the relative amplitudes of spectral peaks  
179 are slight different; this difference is linked to the parameters used in each astronomical  
180 model (detailed in Laskar et al., 2011a). At the low frequencies, amplitude spectrum (Fig. 4b)  
181 shows peaks around the 400-kyr band, i.e.,  $(g_2 - g_5)$  and  $(g_2 - g_5) \pm (g_4 - g_3)$  terms



182 composed of the three periods 405 kyr for  $(g_2 - g_5)$ , 489 kyr for  $(g_2 - g_5) - (g_4 - g_3)$ , and  
183 345 kyr for  $(g_2 - g_5) + (g_4 - g_3)$  (Fig. 4, see Laskar et al., 2004, their table 6). The  
184 interference of the two coupled periods (405 with 345 kyr, and 405 with 489 kyr) induces the  
185 long  $\sim 2.4$  myr eccentricity term, i.e.,  $(g_4 - g_3)$ , which is represented by a significant peak  
186 (Fig. 4b, see Section 3.2.1). Two other main peaks at 670 and 959 kyr correspond  
187 respectively to  $(g_2 - g_1)$  and  $(g_1 - g_5)$  terms. Finally, a weak peak centered on the period of  
188  $\sim 4.5$  myr corresponds to another eccentricity term discussed in Section 3.2.1.

189

190 Lowpass filtering does not show significant low-frequency (longer than  $\sim 4.5$  myr)  
191 variations given that, if present, they are with very low energy as illustrated in the amplitude  
192 spectra (Fig. 4b). Nevertheless, low-amplitude astronomical variations could have significant  
193 influence on Earth's climate change. As an example, though the direct effect of eccentricity  
194 forcing on insolation is relatively low, the strong imprint of the main eccentricity cycles (the  
195 average 97, 128 kyr, and the strong single 405 kyr; Fig. 4a) in paleoclimatic variations could  
196 be indirect, i.e., via energy transfer from the carrier climatic precession into the modulator  
197 eccentricity. Same behavior could manifest in the very low-frequency eccentricity terms  
198 (Section 3.2.1), where energy could be transferred from higher to lower frequency terms via  
199 amplitude/frequency modulation, and all eccentricity terms modulate, in turn, the precession  
200 index cycles. The most compelling example is that the  $\sim 2.4$  myr eccentricity term  $(g_4 - g_3)$   
201 with relatively low amplitude (e.g., Laskar et al., 2004) is well recognized in geological  
202 records (Olsen and Kent, 1999; Hilgen et al., 2003; van Dam et al., 2006; Mitchell et al.,  
203 2008; Abels et al., 2010; and many others), while it could act as a modulator of higher  
204 frequency eccentricity terms, either at the 100 k.y. or at the 400 k.y. cycle bands (e.g., 405  
205 with 489 kyr, and 405 with 345 kyr, Fig. 4b, Section 3.2.1). Another striking example  
206 concerns the Earth's obliquity variations. In particular, the  $\sim 1.2$  myr obliquity cycle is strongly  
207 documented in Cenozoic icehouse strata (e.g., Wade and Pälike, 2004; Pälike et al., 2006a),  
208 although it only acts as a modulator of the higher frequency obliquity cycles (i.e.,  $p + s_3 \approx 41$

209 kyr and  $p + s_4 \approx 39.6$  kyr). Thus, these examples indicate that the presence of a long-period  
210 astronomical cycle with low amplitude, but with a strong imprint in a paleoclimatic record is  
211 possible via amplitude/frequency modulation of the higher frequency cycles, and the  
212 consequent energy-transfer process. Therefore, we tested possible very long-period  
213 eccentricity cycles via amplitude modulation (AM) technique.

214 We performed AM analysis on both the raw  $\delta^{13}\text{C}$  data and the orbital eccentricity, in order to  
215 seek possible analogs. We focused on the  $\sim 400$ -kyr and  $\sim 2.4$ -myr cycles because of their  
216 strength in the  $\delta^{13}\text{C}$  record (Fig. 2a), even if they seem to be biased by the stacked sampling  
217 rates (Figs. 3c,d), and low resolution of the early Cenozoic  $\delta^{13}\text{C}$  data (Fig. S3).

218

## 219 **3.2. Amplitude modulation (AM) analysis**

220

221 First, we bandpass-filtered the orbital eccentricity  $\sim 100$ -kyr,  $\sim 400$ -kyr and  $\sim 2.4$ -myr  
222 variations, and performed Hilbert transforms (e.g., p. 435 in Hinnov, 2000) on the filtered  
223 series (Fig. 1). Then, we applied the same procedure to the  $\delta^{13}\text{C}$  record, but only at the  
224 longer periods, i.e.  $\sim 400$ -kyr and  $\sim 2.4$ -myr (Fig. S3), because the  $\delta^{13}\text{C}$  data resolution is too  
225 low to adequately recover  $\sim 100$ -kyr scale behavior through the past 65 Ma, and the stacked  
226 sampling rates have a significant effect on higher frequency band (Figs. 3c,d; Section 3.1).  
227 Finally, we applied spectral analysis on the amplitude modulation (AM) envelopes (Figs. 5  
228 and 6).

229

### 230 **3.2.1. AM of the orbital eccentricity**

231

232 Time-series analysis of astronomical AM envelopes shows significant long-term  
233 modulations in the eccentricity bands. The AM envelope of the short eccentricity ( $\sim 100$ -kyr)  
234 shows strong 0.405- and 2.4-myrcycles modulations (Fig. 5a), whereas those of the  $\sim 400$ -kyr

235 eccentricity shows strong  $\sim 2.4$ -myr and lesser  $\sim 4.5$ -myr modulations (Figs. 5b and S4). The  
236 AM envelope of the  $\sim 2.4$ -myr orbital eccentricity band shows  $\sim 9$ -myr and  $\sim 26$ -myr cyclicity  
237 (Figs. 5c,d). The latter is not obvious in the AM time series. However, the former is well  
238 detected in AM time series, and shows some correlation with the  $\delta^{13}\text{C}$  record (Section 4).  
239 Thus, the  $\sim 4.5$ - and  $\sim 9$ -myr cyclicities are present in the orbital eccentricity modulations. The  
240  $\sim 2.4$ -myr component could derive from the interference of the two coupled close frequencies  
241 in the 400 kyr band (Fig. 4b). In particular, the interferences of 405 kyr ( $g_2 - g_5$ ) with 345 kyr  
242 ( $(g_2 - g_5) + (g_4 - g_3)$ ), and 405 kyr ( $g_2 - g_5$ ) with 489 kyr ( $(g_2 - g_5) - (g_4 - g_3)$ ) induce both  
243 the 2.4 myr term ( $g_4 - g_3$ ) (see Fig. 4b). The astronomical origin of the  $\sim 4.5$ -myr cycles was  
244 discussed in Laskar (1990) as deriving from the resonant argument  $\theta = 2(g_4 - g_3) - (s_4 - s_3)$ ,  
245 where  $g_3, g_4$  are related to the precession of the perihelions of the Earth and Mars,  $s_3, s_4$  are  
246 related to the precession of the nodes of the same planets. The  $\sim 4.5$ -myr cyclicity is present  
247 in the orbital eccentricity solution (Fig. S5). However, the  $\sim 9$ -myr was not previously  
248 explicated in the astronomical models.

249

### 250 3.2.2. AM of the $\delta^{13}\text{C}$ variations

251

252 Then, we performed  $\sim 400$ -kyr and  $\sim 2.4$ -myr AM analysis on the  $\delta^{13}\text{C}$  records of  
253 Zachos et al.'s (2008) and Cramer et al.'s (2009) compilations (Figs. 6 and S3). The  
254 spectrum of  $\sim 400$ -kyr AM of Zachos et al.'s compilation (Fig. 6a) shows a strong significant  
255 peak centered on 5 myr, and two other weaker but significant peaks of periods 3.8 and 1.9  
256 myr. The 5- and 3.8-my peaks may represent the average of the  $\sim 4.5$ -myr periodicity  
257 (discussed previously). The 1.9 myr peak could represent a distorted  $\sim 2.4$ -myr eccentricity  
258 modulation term (see below). The spectrum of  $\sim 400$ -kyr AM of Cramer et al.'s compilation  
259 (Fig. 6b) indicates two strong significant peaks centered on 2.4 and 16 myr. The former

260 corresponds likely to 'g4-g3' eccentricity term (Fig. 5b). However, the latter is not evident  
261 neither in the astronomical variations nor in the  $\delta^{13}\text{C}$  time series.

262

263 The spectrum of  $\sim 2.4$ -myr AM of Zachos et al.'s compilation (Fig. 6c) shows mainly four  
264 significant peaks (above 99% CL) centered on the periods of 6.3, 8.1, 12, and 32 myr. The  
265 three first ones, with an average of 8.8 myr, may represent the  $\sim 9$  myr astronomical  
266 variations. The latter again is not evident in the  $\delta^{13}\text{C}$  time series. The spectrum of  $\sim 2.4$ -myr  
267 AM of Cramer et al.'s compilation (Fig. 6d) highlights three significant peaks centered on the  
268 periods of 7.4, 10.2, and 27.5 myr. The former two, with an average of 8.8 myr, most likely  
269 represent the  $\sim 9$  myr astronomical variations. The latter may represent the peak seen in the  
270 raw  $\delta^{13}\text{C}$  spectrum (i.e., 29 myr, Fig. 3b). Therefore, AM results suggest that the  $\sim 9$ -myr  
271 cyclicity modulates the  $\sim 2.4$ -myr and not the  $\sim 400$ -kyr cycles as has been demonstrated in  
272 the astronomical models. Additionally, AM results of the 2.4 myr band is more consistent  
273 than those of the 400 kyr band. This again suggests the more effect of sampling rates on  
274 higher frequency cycles. In sum, despite of the Cramer et al.'s (2009) compilation show  
275 some  $\delta^{13}\text{C}$  frequencies, in the  $\sim 2.4$ -myr AM, consistent with astronomical frequencies, the  
276 large differences of AM outputs (Figs. 6 and S3) between the two  $\delta^{13}\text{C}$  versions (Zachos et  
277 al., 2008; Cramer et al., 2009) preclude any positive conclusion regarding AM results. The  
278 stacked sampling rates could be the most important factor that affects the documentation of  
279 higher frequency cycles, and hence AM use, given that both  $\delta^{13}\text{C}$  compilations are rescaled  
280 to the same timescale (GTS2004, Gradstein et al., 2004). Nevertheless, the  $\sim 9$  myr cycles  
281 are prominent and robust in both  $\delta^{13}\text{C}$  compilations.

282

#### 283 4. $\delta^{13}\text{C}$ variations and orbital eccentricity correlation

284

285           The 9-myrcentricity cycles correlate well with the raw  $\delta^{13}\text{C}$  (Fig. 1) because of the  
286 higher sensitivity of global carbon-cycle to eccentricity forcing (e.g., Cramer et al., 2003;  
287 Pälike et al., 2006a; Abels et al., 2010). A clear negative correlation between eccentricity and  
288  $\delta^{13}\text{C}$  cycles was observed from ~8 to ~60 Ma. Maxima of  $\delta^{13}\text{C}$  correspond to minima of ~9  
289 myrcentricity cycles. Similar negative correlation was also demonstrated at the higher  
290 frequency eccentricity cycles (~2.4-myrc, ~400-kyrc, and ~100-kyrc, Cramer et al., 2003; Pälike  
291 et al., 2006a, and many others). Cb1 to Cb8  $\delta^{13}\text{C}$  cycles correlate well with the ~9 myrc  
292 astronomical cycles (Fig. 7). The average cross phase estimate between ~2.4-myrc  
293 eccentricity AM and ~9 myrc  $\delta^{13}\text{C}$  cycles is about -180 degrees (Fig. 7). This supports the  
294 antiphase relationship between eccentricity and  $\delta^{13}\text{C}$  variations. However, visual examination  
295 of the time series (Fig. 1, Cuves 3 and 4) indicates that  $\delta^{13}\text{C}$  and eccentricity variations are  
296 sometimes phase-shifted at the ~9 myrc cyclicity suggesting that non-orbital processes (e.g.,  
297 tectonics) could interfere into these long-term  $\delta^{13}\text{C}$  oscillations (e.g., Zachos et al., 2001;  
298 Leckie et al., 2002; Li et al., 2009). On the other hand, La2004 astronomical model (Laskar et  
299 al., 2004) is valid for only the last 40 Ma, while the La2010d model (Laskar et al., 2011a) is  
300 reliable for the last 50 Ma. Thus, correlation between  $\delta^{13}\text{C}$  and astronomical variations for the  
301 interval 50 to 67 Ma (Cb7 and Cb8) is critical, and should be considered with caution till a  
302 future extended astronomical model will be available, and future studies could enhance  
303 geological timescale resolution.

304

305           Besides, we note a positive correlation between  $\delta^{13}\text{C}$  and astronomy for the last ~8  
306 Ma. This exception may be due to the compilation of the carbon isotopes data itself, which  
307 should be checked in future  $\delta^{13}\text{C}$  compilations. In fact, possible unreliable  $\delta^{13}\text{C}$  compiled data  
308 could exist for the Plio-Pleistocene where basin to basin fractionation develops (low values of  
309 the Pacific, J. Zachos, *pers. comm*). Recent studies concur with this hypothesis, and show  
310 that Atlantic-Pacific  $\delta^{13}\text{C}$  differential responses exist for the last ~10 Ma (Cramer et al., 2009,

311 their figure 6). A different hypothesis, Wang et al. (2010) suggested that the expression of  
312 eccentricity in the  $\delta^{13}\text{C}$  record is obscured for at least the last  $\sim 1.6$  Ma, related to a major  
313 change in the oceanic carbon reservoir associated with a restructuring of the Southern  
314 Ocean. Finally, Katz et al. (2005) interpreted a long-term linear trend in this interval (precisely  
315 for the last  $\sim 17$  Ma, in their figure 1) as the result of a closing phase of the Wilson cycle,  
316 when continents reassemble and the Atlantic Ocean basin closes. According to these  
317 observations, we restrict our interpretation, in terms of possible orbital forcing of the 9-myrr  
318  $\delta^{13}\text{C}$  cycles, to the interval  $\sim 8$  to  $\sim 50$  Ma, and with caution the interval  $\sim 50$  to  $\sim 60$  Ma, where  
319 9-myrr  $\delta^{13}\text{C}$  and eccentricity cycles are anticorrelated.

320

## 321 **5. Discussion: how does orbital forcing drive Cenozoic carbon cyclicity?**

322

323 High-amplitude (1‰) eccentricity-scale cyclicity has been described in various upper  
324 Paleocene-Neogene  $\delta^{13}\text{C}$  records (Woodruff and Savin, 1991; Flower and Kennett, 1995;  
325 Diester-Haass, 1996; Zachos et al., 1996, 1997, 2001; Cramer et al., 2003; Pälike et al.,  
326 2006a,b), suggesting that carbon recycling through the atmosphere-biosphere-ocean  
327 reservoir (e.g., Siegenthaler and Sarmiento, 1993; Sarmiento and Bender, 1994)  
328 preferentially responds to orbital eccentricity from modulation of the climatic precession. For  
329 example, by applying climatic precession forcing to carbonate/organic carbon fluxes and  
330 deposition, and the residence-time of carbon in the atmosphere-biosphere-ocean, Cramer et  
331 al. (2003) modelled a theoretical eccentricity curve consistent with interpreted eccentricity  
332 cycles ( $\sim 100$  and  $\sim 400$  kyr) in their measured bulk carbonate  $\delta^{13}\text{C}$ . Specifically, they showed  
333 a correspondence between maxima in  $\sim 400$ -kyr eccentricity and transient decreases in the  
334 bulk carbonate  $\delta^{13}\text{C}$  during the late Paleocene - early Eocene. In another example from the  
335 Oligocene, Pälike et al. (2006a) demonstrated that long-term insolation forcing could  
336 modulate atmospheric  $\text{CO}_2$  levels as well as the oceanic carbonate ion ( $\text{CO}_3^{2-}$ ) concentration,

337 leading to expansion and contraction of biospheric productivity in tune with long-term orbital  
338 periodicities. Specifically, [Pälike et al. \(2006a\)](#) highlighted a strong ~400-kyr signal in the  
339  $\delta^{13}\text{C}$  record, which they explained as the consequence of the long residence-time of carbon  
340 in the oceans, leading to enhanced sensitivity to longer forcing periods.

341 In this study, we show a prominent ~9 myr cyclicity in  $\delta^{13}\text{C}$  record, which may  
342 correspond to ~9 myr AM cycles in orbital eccentricity variations. This is in accordance with  
343 the idea of long residence-time of carbon in amplifying longer orbital periodicities. We also  
344 note that the maxima of long-term  $\delta^{13}\text{C}$  oscillations correspond to minima of long-term  
345 eccentricity modulations ([Figs. 1 and 2a](#)), which again concurs with previous  $\delta^{13}\text{C}$   
346 cyclostratigraphic studies ([Cramer et al., 2003](#); [Pälike et al., 2006a](#), [Rickaby et al., 2007](#); and  
347 many others). Therefore, if there is a link between  $\delta^{13}\text{C}$  record and orbital eccentricity  
348 modulation at this multi-millionyear timescale, and considering previous studies in carbon-  
349 cycle modeling, we could suggest that eccentricity induced insolation through its modulation  
350 of the climatic precession may play an important role in carbon cycling, controlling a chain of  
351 astro-climatically sensitive processes such as terrestrial weathering, biosphere productivity,  
352 carbonate sedimentation and dissolution, burial and oxidation of organic carbon, etc (e.g.,  
353 [Westbroek et al., 1993](#); [Cramer et al., 2003](#); [Kurtz et al., 2003](#); [Pälike et al., 2006a](#); [Rickaby](#)  
354 [et al., 2007](#); [Li et al., 2009](#)). At the same time, observed phase shifts between ~9-myrr  
355 eccentricity and  $\delta^{13}\text{C}$  cycles suggest that additional processes (e.g., tectonics) could  
356 contribute to the  $\delta^{13}\text{C}$  variations.

357

358 Finally, the most prominent ~9-myrr  $\delta^{13}\text{C}$  cycle (Cb7, [Figs. 1 and 2a](#)), which  
359 corresponds to a well expressed ~9-myrr astronomical cycle in the eccentricity modulation,  
360 includes the Paleocene-Eocene Thermal Maximum (PETM) event ([Figs. 1 and 2b](#)). In  
361 particular, the PETM, which corresponds to a pronounced  $\delta^{13}\text{C}$  negative excursion (2.5-3‰),  
362 is situated within a strong decrease in the Cb7  $\delta^{13}\text{C}$  cycle, hinting at a possible link between

363  $\delta^{13}\text{C}$  rates and the occurrence of the event. The Cb7 cycle, especially its decreasing part,  
364 seems to be amplified compared to the other  $\sim 9$  myr  $\delta^{13}\text{C}$  cycles (Fig. 1). This observation is  
365 beyond the scope of our study, and needs, however, future work to model causes of rates in  
366 the  $\delta^{13}\text{C}$  variations and their link with the PETM onset in this specific interval of Cenozoic  
367 (e.g., volcanism: Storey et al., 2007, and J. Zachos, pers. com; methane release from gas  
368 hydrate: Dickens et al., 1995, 1997).

369

370

## 371 **6. Conclusions**

372

373 We show that Cenozoic carbon isotope record ( $\delta^{13}\text{C}$ ) exhibits a multi-millionyear cycle  
374 of a pseudo-periodicity close to 9 myr. Amplitude modulation (AM) analysis of astronomical  
375 models shows that the  $\sim 2.4$  myr eccentricity cycles are mainly modulated by  $\sim 9$  myr cycles  
376 similar to those observed in the  $\delta^{13}\text{C}$  record. Several lines of correlation are observed  
377 between  $\sim 9$  myr eccentricity envelopes and  $\delta^{13}\text{C}$  cycles pointing to a possible link between  
378 the two.

379 Additionally, the Paleocene-Eocene Thermal Maximum (PETM) event, which  
380 corresponds to a pronounced  $\delta^{13}\text{C}$  negative excursion, coincides with a critical interval in the  
381  $\sim 9$  myr  $\delta^{13}\text{C}$  cycle. An unusual strong decrease in the most prominent  $\sim 9$  myr  $\delta^{13}\text{C}$  of the  
382 Cenozoic may reflect specific processes in atmosphere-continent-ocean system (e.g.,  
383 methane release from gas hydrate, volcanism), responsible for the amplification of the  $\sim 9$   
384 myr  $\delta^{13}\text{C}$  cycle and the PETM excursion.

385

386

## 387 **Acknowledgments**

388



389 J. Laskar, B. Galbrun, and S. Boulila were supported by French ANR Grant ASTS-CM. J.  
390 Laskar acknowledge the support from GENCI-CINES and PNP-CNRS. S. Boulila thanks  
391 Linda Hinnov for help in time-series analysis and her revisions and comments on an earlier  
392 version of the manuscript. We also thank Jim Zachos for help of the revised stable isotopes  
393 data, and his comments and revisions on an earlier version of the manuscript. S. Boulila  
394 thanks very much Jim Ogg (Purdue University) for help in geological timescale conversion.

395

396

### 397 **References**

398

399 Abels, H.A., Abdul Aziz, H., Krijgsman, W., Smeets, S.J.B., Hilgen, F.J., 2010. Long-period  
400 eccentricity control on sedimentary sequences in the continental Madrid Basin (middle  
401 Miocene, Spain). *Earth Planet. Sci. Lett.* 289, 220–231.

402 Archer, D., Maier-Reimer, E., 1994. Effect of deep-sea sedimentary calcite preservation on  
403 atmospheric CO<sub>2</sub> concentration. *Nature* 367, 260–263.

404 Berger, A., Loutre, M.F., Laskar, J., 1992. Stability of the Astronomical Frequencies Over the  
405 Earth's History for Paleoclimate Studies. *Science* 255, 560–566.

406 Billups, K., Pälike, H., Channell, J.E.T., Zachos, J.C., Shackleton, N.J., 2004. Astronomic  
407 calibration of the late Oligocene through early Miocene geomagnetic polarity time scale.  
408 *Earth Planet. Sci. Lett.* 224, 33–44.

409 Charles, A.J., Condon, D.J., Harding, I.C., Pälike, H., Marshall, J.E.A., Cui, Y., Kump, L.,  
410 Croudace, I.W., in press. Constraints on the numerical age of the Paleocene/Eocene  
411 boundary. <http://www.agu.org/journals/pip/gc/2010GC003426-pip.pdf>

412 Cramer, B.S., Wright, J.D., Kent, D.V., Aubry, M.P., 2003. Orbital climate forcing of d<sup>13</sup>C  
413 excursions in the late Paleocene–Eocene (Chronos C24n–C25n). *Paleoceanography*  
414 18(4), 1097, doi: 10.1029/2003PA000909.

415 Cramer, B.S., Toggweiler, J.R., Wright, J.D., Katz, M.E., Miller, K.G., 2009. Ocean  
416 overturning since the Late Cretaceous: Inferences from a new benthic foraminiferal  
417 isotope compilation. *Paleoceanography* 24, PA4216, doi: 10.1029/2008PA001683.

418 Dickens, G.R., Castillo, M.M., Walker, J.C.G., 1997. A blast of gas in the latest Paleocene:  
419 Simulating first order effects of massive dissociation of oceanic methane hydrate.  
420 *Geology* 25, 259–262.

421 Dickens, G.R., O'Neil, J.R., Rea, D.K., Owen, R.M., 1995. Dissociation of oceanic methane  
422 hydrate as a cause of the carbon isotope excursion at the end of the Paleocene.  
423 *Paleoceanography* 10, 965–971.

424 Diester-Haass, L., 1996. Late Eocene-Oligocene paleoceanography in the southern Indian  
425 Ocean (ODP Site 744). *Mar. Geol.* 130, 99–119.

426 Fienga, A., Manche, H., Laskar, J., Gastineau, M., 2008. INPOP06. A new numerical  
427 planetary ephemeris. *Astron. Astrophys.* 477, 315–327.

428 Fienga, A., Laskar, J., Morley, T., Manche, H., Kuchynka, P., Le Poncin-Lafitte, C., Budnik,  
429 F., Gastineau, M., Somenzi, L., 2009. INPOP08, a 4-D planetary ephemeris: from  
430 asteroid and time-scale computations to ESA Mars Express and Venus Express  
431 contributions. *Astron. Astrophys.* 507, 1675–1686.

432 Flower, B., Kennett, J., 1995. Middle Miocene deepwater paleoceanography in the southwest  
433 Pacific: Relations with East Antarctic Ice Sheet development. *Paleoceanography* 10,  
434 1095–1112.

435 Forte, A.M., Mitrovica, J.X., 1997. A resonance in Earth's obliquity and precession over the  
436 past 20 Myr driven by mantle convection. *Nature* 390, 676–680.

437 Ghil, M., Allen, R.M., Dettinger, M.D., Ide, K., Kondrashov, D., Mann, M.E., Robertson, A.,  
438 Saunders, A., Tian, Y., Varadi, F., Yiou, P., 2002. Advanced spectral methods for climatic  
439 time series. *Rev. Geophys.* 40 (1), 3.1–3.41.

440 Gradstein, F.M., Ogg, J.G., Smith, A.G., 2004. *A Geologic Time Scale 2004*. Cambridge  
441 University Press, 589 p.

442 Hays, J. D., Imbrie, J., Shackleton, N.J., 1976. Variations in the earth's orbit: pacemaker of  
443 the ice ages. *Science* 194, 1121–1132.

444 Hilgen, F.J., Abdul Aziz, H., Krijgsman, W., Raffi, I., Turco, E., 2003. Integrated stratigraphy  
445 and astronomical tuning of the Serravallian and lower Tortonian at Monte dei Corvi  
446 (Middle-Upper Miocene, northern Italy). *Palaeogeogr. Palaeoclimatol. Palaeoecol.* 199,  
447 229–264.

448 Hinnov, L.A., 2000. New perspectives on orbital stratigraphy. *Ann. Rev. Earth Planet. Sci.* 28,  
449 419–475.

450 Huybers, P., Denton, G., 2008. Antarctic temperature at orbital time scales controlled by local  
451 summer duration. *Nature Geoscience* 1, 787–792.

452 Imbrie, J., Hays, J.D., Martinson, D.G., McIntyre, A., Mix, A.C., Morley, J.J., Pisias, N.G.,  
453 Prell, W.L., Shackleton, N.J., 1984. The orbital theory of Pleistocene climate: support  
454 from a revised chronology of the marine  $\delta^{18}\text{O}$  record. *In: Berger A. et al. (eds.),*  
455 *Milankovitch and climate. Understanding the response to astronomical forcing NATO.*  
456 *Advanced Science Institutes Series C.* 126, 269-305.

457 Katz, M.E., Wright, J.D., Miller, K.G., Cramer, B., Fennel, K., Falkowski, P.G., 2005.  
458 Biological overprint of the global carbon cycle. *Mar. Geol.* 217, 323–338.

459 Kuiper, K.F., Deino, A., Hilgen, F.J., Krijgsman, W., Renne, P.R., Wijbrans, J.R., 2008.  
460 Synchronizing Rock Clocks of Earth History. *Science* 320, 500-504.

461 Kurtz, A.C., Kump, L.R., Arthur, M.A., Zachos, J.C., Paytan, A., 2003. Early Cenozoic  
462 decoupling of the global carbon and sulfur cycles. *Paleoceanography* 18, doi:  
463 10.1029/2003PA000908.

464 Lagabrielle, Y., Godd ris, Y., Donnadi u, Y., Malavieille, J., Suarez, M., 2009. The tectonic  
465 history of Drake Passage and its possible impacts on global climate. *Earth Planet. Sci.*  
466 *Lett.* 279, 197–211.

467 Laskar J., 1990. The chaotic motion of the Solar System: A numerical estimate of the size of  
468 the chaotic zone. *Icarus* 88, 266–291.

469 Laskar J., 1992. The limits of the Earth orbital calculations for geological time-scale use.  
470 Royal Soc. (London), *Phil. Trans. Ser. A* 357, 1735–1759.

471 Laskar J., Fienga A., Gastineau M., Manche H., 2011a. La2010: A new orbital solution for the  
472 long term motion of the Earth. *Astron. Astrophys.* 532, A89, doi: 10.1051/0004-  
473 6361/201116836.

474 Laskar, J., Gastineau, M., Delisle, J.-B., Farrés, A., Fienga, A., 2011b. Strong chaos induced  
475 by close encounters with Ceres and Vesta *Astron. Astrophys.*, in press, manuscript no.  
476 17504R.

477 Laskar J, Joutel F., Boudin F., 1993. Orbital, precessional, and insolation quantities for the  
478 Earth from -20 Myr to + 10 Myr. *Astron. Astrophys.* 270, 522–533.

479 Laskar J., Robutel P., Joutel F., Gastineau M., Correia A. C. M., Lestrade B., 2004. A long-  
480 term numerical solution for the insolation quantities of the Earth. *Astron. Astrophys.* 428,  
481 261–285.

482 Leckie, R.M., Bralower, T., Cashman, R., 2002. Oceanic anoxic events and plankton  
483 evolution: Biotic response to tectonic forcing during the mid-Cretaceous.  
484 *Paleoceanography* 17(3), doi: 10.1029/2001PA000623.

485 Li, G., Ji, J., Chen, J., Kemp, D.B., 2009. Evolution of the Cenozoic carbon cycle: The roles of  
486 tectonics and CO<sub>2</sub> fertilization. *Glob. Biogeochem. Cycles* 23, GB1009, doi:  
487 10.1029/2008GB003220.

488 Lourens, L.J., Sluijs, A., Kroon, D., Zachos, J.C., Thomas, E., Röhl U., Bowles, J., Raffi, I.,  
489 2005. Astronomical pacing of late Palaeocene to early Eocene global warming events.  
490 *Nature* 435, 1083–108.

491 Mann, M.E., Lees, J.M., 1996. Robust estimation of background noise and signal detection  
492 in climatic time series. *Clim. Change* 33, 409–445.

493 Mitchell, R.N., Bice, D.M., Montanari, A., Cleavel, L.C., Christianson, K.T., Coccioni, R.,  
494 Hinnov, L.A., 2008. Oceanic Anoxic Cycles? Orbital prelude to the Bonarelli Level (OAE  
495 2). *Earth Planet. Sci. Lett.* 267, 1–16.

496 Mitrovica, J.X., Forte, A.M., Pan, R., 1997. Glaciation-induced variations in the Earth's  
497 precession frequency, obliquity and insolation over the last 2.6 Ma. *Geophys. J. Intern.*  
498 128(2), 270–284.

499 Olsen, P.E., Kent, D.V., 1999. Long-term Milankovitch cycles from the Late Triassic and  
500 Early Jurassic of eastern North America and their implications for the calibration of the  
501 Early Mesozoic timescale and the long term behavior of the planets. *Royal Soc.*  
502 (London), *Phil. Trans. Ser. A.* 357,1761–1788.

503 Paillard, D., Labeyrie, L., Yiou, P, 1996. Macintosh program performs timeseries analysis.  
504 *Eos* 77, 379.

505 Pälike, H., Frazier, J., Zachos, J.C., 2006b. Extended orbitally forced palaeoclimatic records  
506 from the equatorial Atlantic Ceara Rise. *Quat. Sci. Rev.* 25, 3138–3149.

507 Pälike, H., Laskar, J., Shackleton, N.J., 2004. Geologic constraints on the chaotic diffusion of  
508 the Solar System. *Geology* 32, 929–932.

509 Pälike, H., Norris, R.D., Herrle, J.O., Wilson, P.A., Coxall, H.K., Lear, C.H., Shackleton, N.J.,  
510 Tripathi, A.K., Wade, B.S., 2006a. The Heartbeat of the Oligocene Climate System.  
511 *Science* 314, 1894–1898.

512 Raymo, M.E., Ruddiman, W.F., 1992. Tectonic forcing of late Cenozoic climate. *Nature* 359,  
513 117–122.

514 Rickaby, R.E.M., Bard, E., Sonzogni, C., Rostek, F., Beaufort, L., Braker, S., Rees, G.,  
515 Schrag, D.P., 2007. Coccolith chemistry reveals secular variations in the global ocean  
516 carbon cycle?. *Earth Planet. Sci. Lett.* 235, 83–95.

517 Sarmiento, J., Bender, M., 1994. Carbon biogeochemistry and climate change. *Photosyn.*  
518 *Res.* 39, 209–234.

519 Shackleton, N.J., Crowhurst, S.J., Weedon, G.P., Laskar, J., 1999. Astronomical calibration  
520 of Oligocene-Miocene time. *Philos. Trans. R. Soc. London A* 357, 1907–1929.

521 Siegenthaler, U., Sarmiento, J., 1993. Atmospheric carbon dioxide and the ocean. *Nature*  
522 365, 119–125.

523 Standish, E.M., 1998. JPL Planetary and Lunar Ephemerides, DE405/LE405. Jet Propulsion  
524 Laboratory, Interoffice Memorandum, IOM 312.F – 98 – 048.

525 Storey, M., Duncan, R.A., III, C.C., 2007. Paleocene-Eocene Thermal Maximum and the  
526 Opening of the Northeast Atlantic. *Science* 316, 587–589.

527 Thomson, D.J., 1982. Spectrum estimation and harmonic analysis. *IEEE Proc.* 70, 1055–  
528 1096.

529 van Dam, J.A., Abdul, Aziz, H., Sierra, M.A.A., Hilgen, F.J., van den Hoek Ostende, L.W.,  
530 Lourens, L.J., Mein, P., van der Meulen, A.J., and Pelaez-Campomanes, P., 2006. Long-  
531 period astronomical forcing of mammal turnover. *Nature* 443, 687–691.

532 Wade, B.S., Pälike, H., 2004. Oligocene climate dynamics. *Paleoceanography* 19, PA4019,  
533 doi: 10.1029/2004PA001042.

534 Westbroek, P., Brown, C.W., Vanbleijswijk, J., Brownlee, C., Brummer, G.J., Conte, M.,  
535 Egge, J., Fernandez, E., Jordan, R., Knappertsbusch, M., Stefels, J., Veldhuis, M.,  
536 Vanderwal, P., Young, J., 1993. A model system approach to biological climate forcing:  
537 the example of *Emiliana huxleyi*. *Glob. Planet. Change* 8, 27–46.

538 Westerhold, T., Röhl, U., Laskar, J., Raffi, I., Bowles, J., Lourens, L.J., Zachos, J.C., 2007.  
539 On the duration of Magnetochrons C24r and C25n, and the timing of early Eocene global  
540 warming events: Implications from the ODP Leg 208 Walvis Ridge depth transect.  
541 *Paleoceanography* 22(PA2201): doi:10.1029/2006PA001322.

542 Westerhold, T., Röhl, U., McCarren, H.K., Zachos, J.C., 2009. Latest on the absolute age of  
543 the Paleocene – Eocene Thermal Maximum (PETM): new insights from exact  
544 stratigraphic position of key ash layers +19 and -17. *Earth Planet. Sci. Lett.* 287, 412–  
545 419.

546 Westerhold, T., Röhl, U., Raffi, I., Fornaciari, E., Monechi, S., Reale, V., Bowles, J., Evans,  
547 H.F., 2008. Astronomical calibration of the Paleocene time. *Palaeogeogr.*  
548 *Palaeoclimatol. Palaeoecol.* 257, 377–403.

549 Woodruff, F., Savin, S., 1991. Mid-Miocene isotope stratigraphy in the deep sea: High-  
550 resolution correlations, paleoclimatic cycles, and sediment preservation.  
551 *Paleoceanography* 6, 755–806.

552 Zachos, J.C., Dickens, G.R., Zeebe R.E., 2008. An early Cenozoic perspective on  
553 greenhouse warming and carbon-cycle dynamics. *Nature* 451, 279–283.

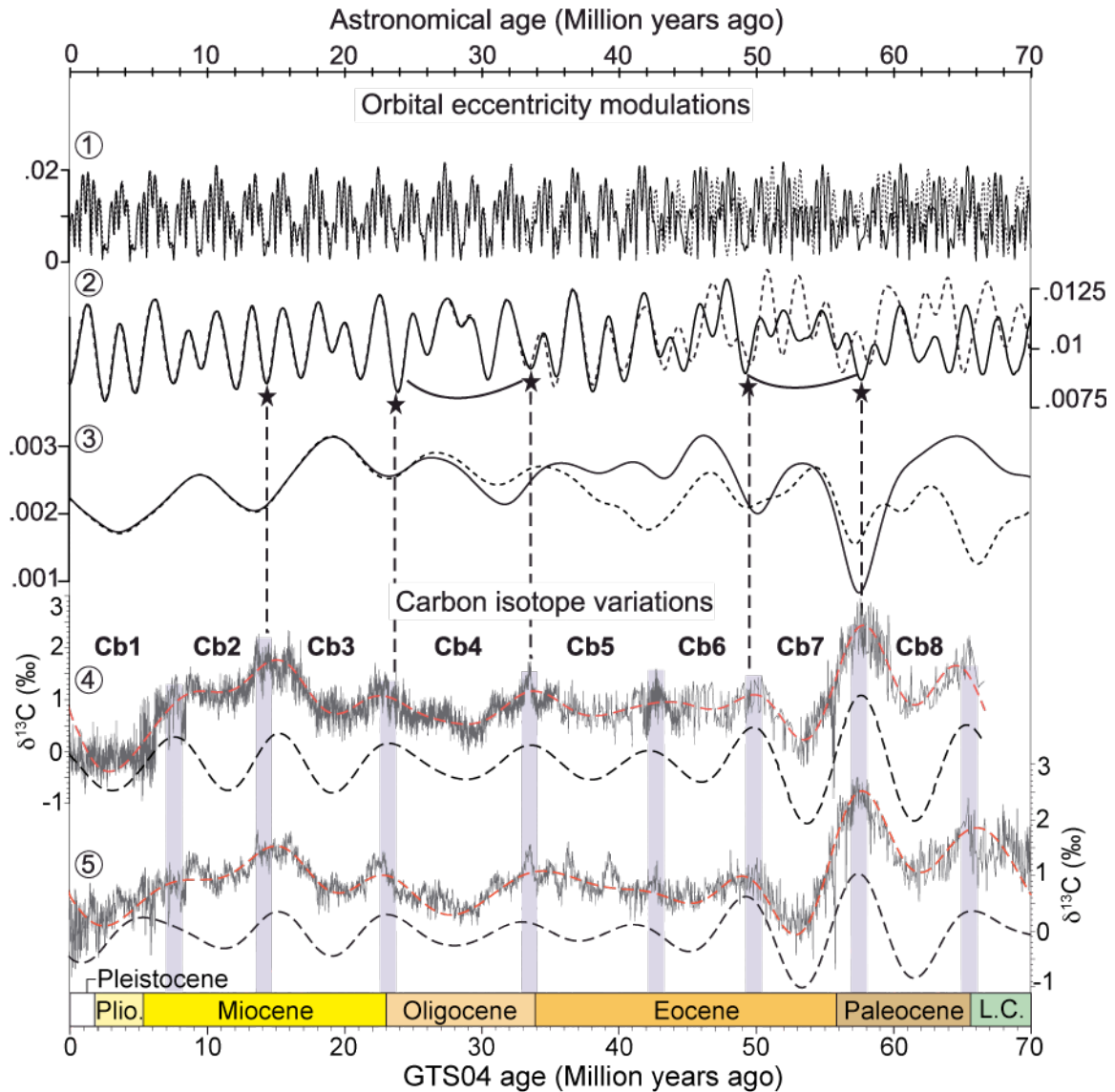
554 Zachos, J.C., Flower, B., Paul, H., 1997. Orbitally paced climate oscillations across the  
555 Oligocene/Miocene boundary. *Nature* 388, 567–570.

556 Zachos, J.C., Pagani, M., Sloan, L., Thomas, E., Billups, K., 2001. Trends, Rhythms,  
557 Aberrations in Global Climate 65 Ma to Present. *Science* 292, 686–693.

558 Zachos, J.C., Quinn, T., Salamy, K., 1996. High-resolution ( $10^4$  years) deep-sea foraminiferal  
559 stable isotope records of the Eocene-Oligocene climate transition. *Paleoceanography*  
560 11, 251–266.

561

562



563

564

**Figure 1:** Amplitude modulations (AM) of the nominal La2004 (solid curves) and La2010d

565

(dashed curves) astronomical models (Laskar et al., 2004, and Laskar et al., 2011a), and

566

correlation with the ~9 myr δ<sup>13</sup>C cyclicity of deep-sea δ<sup>13</sup>C records (Zachos et al., 2001,

567

2008; Cramer et al., 2009). Top to bottom, **curve 1:** AM of the short eccentricity band

568

(9.4 ± 2 myr<sup>-1</sup>), **curve 2:** inverted AM of the ~400-kyr eccentricity band (2.5 ± 0.5 myr<sup>-1</sup>),

569

**curve 3:** AM of the ~2.4-myrcentricity band (0.4245 ± 0.1350 myr<sup>-1</sup>). **curves 4:** raw

570

δ<sup>13</sup>C record (Zachos et al., 2001, 2008), also shown low-pass (0 to 0.17 myr<sup>-1</sup> band) and

571

bandpass (0.1265 ± 0.04245 myr<sup>-1</sup>) filtered δ<sup>13</sup>C record, the ~9-myrc<sup>13</sup>C oscillations are

572

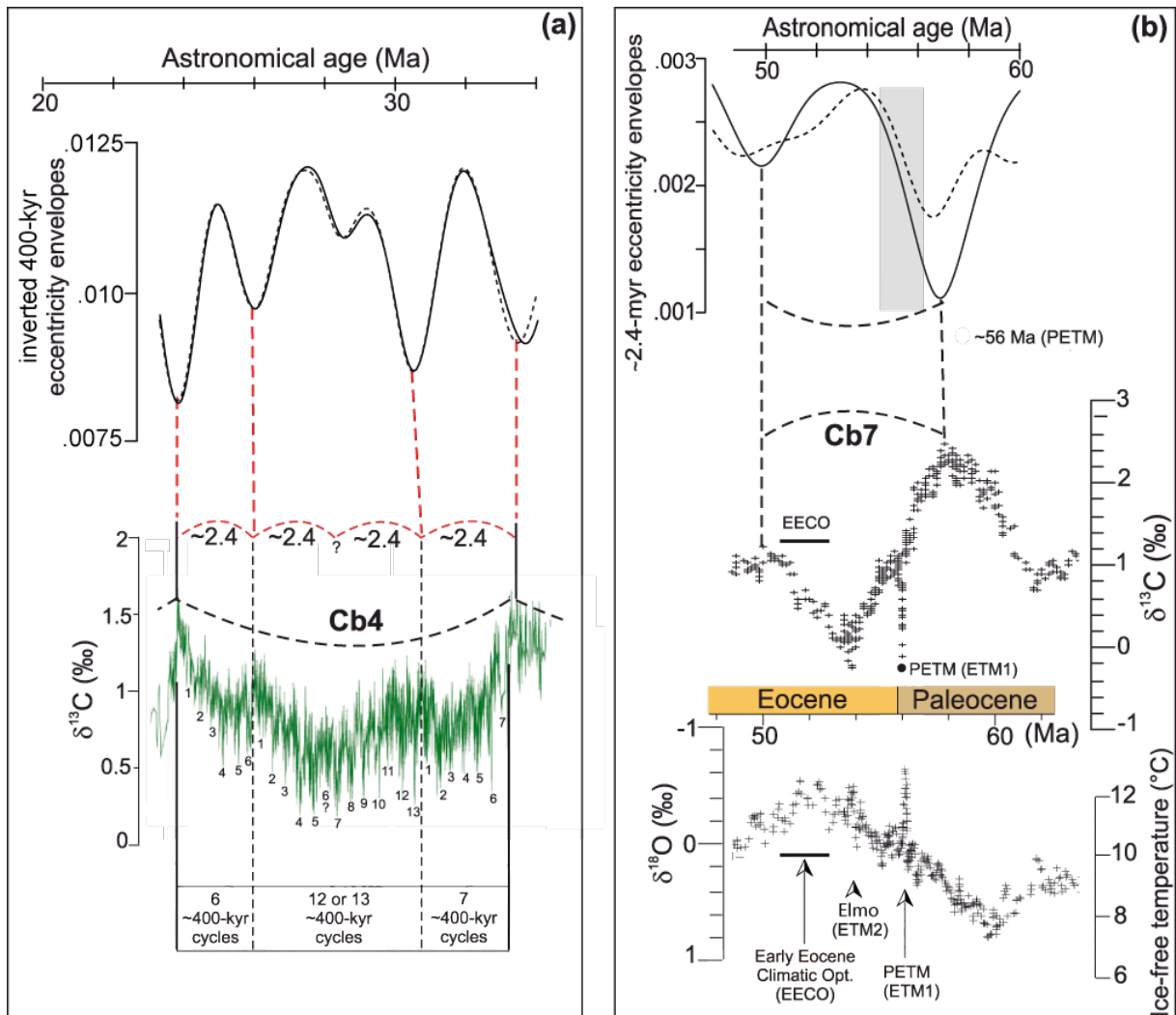
shown (labelled Cb1 to Cb8 delimited by vertical bars), **curves 5:** δ<sup>13</sup>C record (Cramer et

573

al., 2009) with 5 point running average. Low-pass (0 to 0.17 myr<sup>-1</sup> band) and bandpass

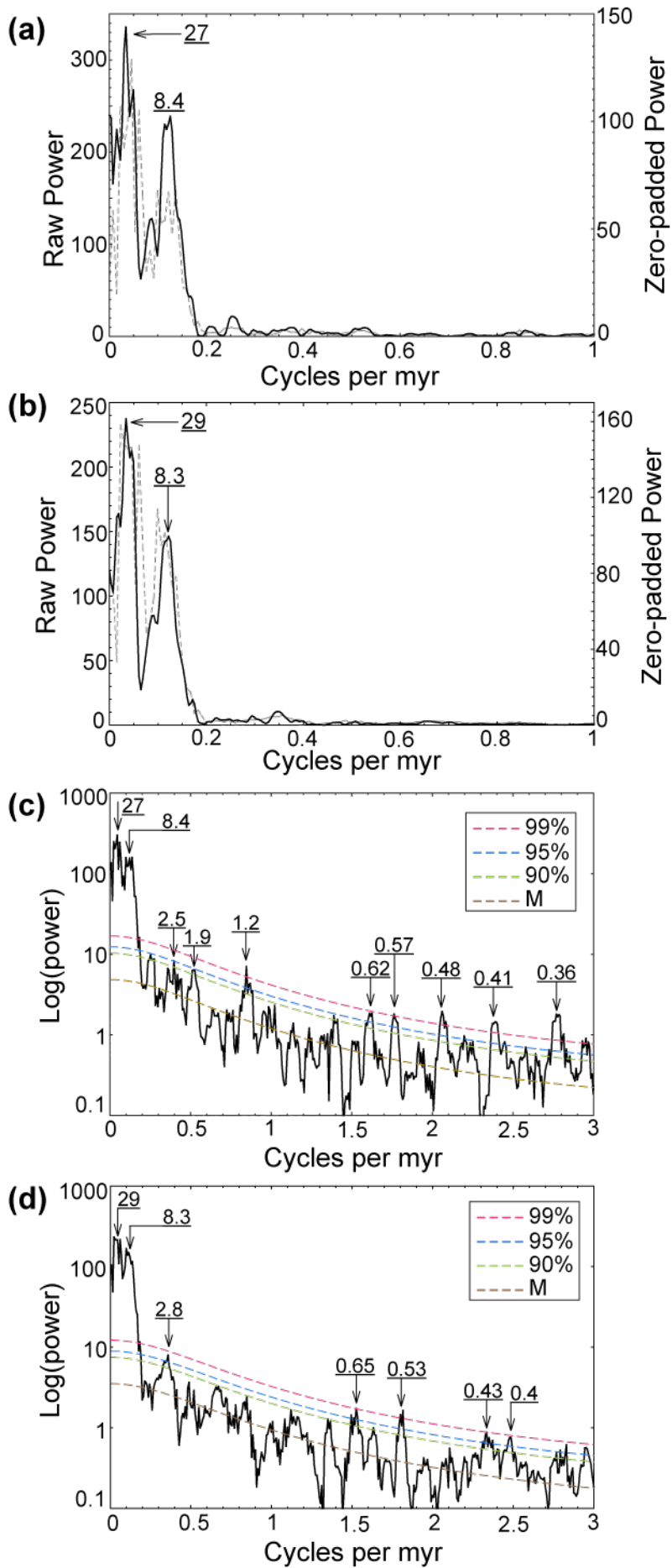


574 (0.1265 ± 0.04245 myr<sup>-1</sup>) filtered  $\delta^{13}\text{C}$  record is also shown, applied to the raw  $\delta^{13}\text{C}$  data  
 575 (resampled to 0.004 myr). For filtering, we used a Gaussian filter (Paillard et al., 1996).  
 576 All filtering in orbital eccentricity was carried out on the -10 to 75 Ma interval to avoid  
 577 filter-edge effect. AM analysis was performed by Hilbert transformation (e.g., p. 435 in  
 578 Hinno, 2000). The vertical dashed lines represent the correlation between the 'Cb'  
 579 cycles and the astronomical ~9-my cycles, with emphasis on five tie-points (represented  
 580 with black stars) which show good correlation of Cb3, Cb4, and Cb7 to their equivalent  
 581 astronomical cycles (vertical dashed lines: possible bundling of four ~2.4 myr cycles).  
 582

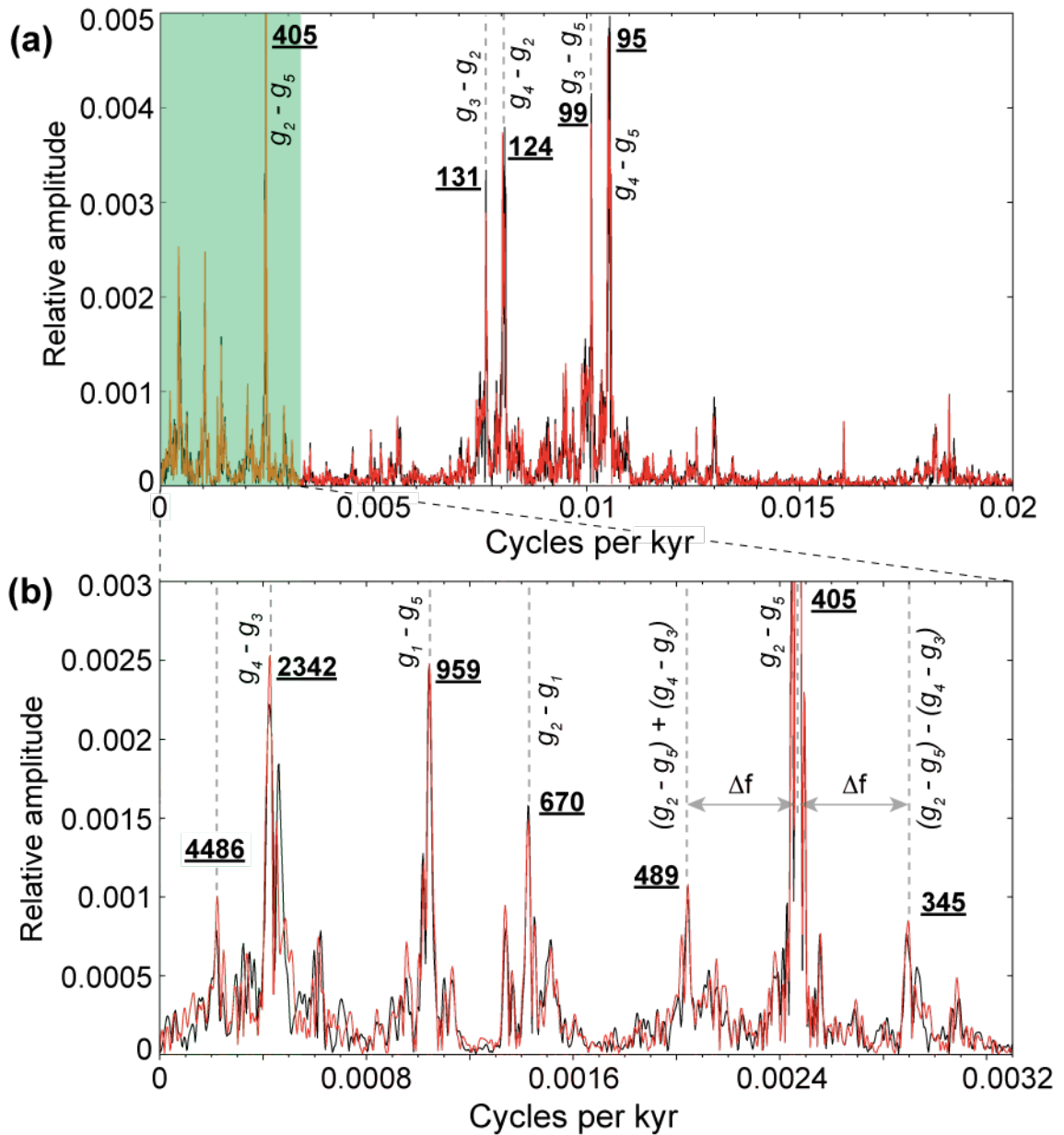


583  
 584 **Figure 2:** Details of ~9-my cycles show a good correlation between  $\delta^{13}\text{C}$  record and AM  
 585 eccentricity, and the position of  $\delta^{13}\text{C}$  brief events ( $\delta^{18}\text{O}$  is also shown, from

586 Supplementary Figure S1). **(a)** The Cb4  $\delta^{13}\text{C}$  cycle correlates to the  $\sim 9$ -myr astronomical  
587 cycle (from Fig. 1, curve 2). The two middle  $\sim 2.4$ -myr cycles are “amalgamated” in both  
588 the  $\delta^{13}\text{C}$  and the astronomical signal. This supports the validity of the astronomical  
589 models. **(b)** The Cb7  $\delta^{13}\text{C}$  cycle correlates to the  $\sim 9$ -myr astronomical cycle (from Fig. 1,  
590 curve 3), but should be considered with caution given that neither the geological time  
591 scale nor the astronomical models are precise in this time interval. The vertical bar  
592 indicates the interval ( $\sim 54.5$  to  $\sim 56.2$  Ma) including the PETM event (56 Ma, estimates  
593 are from [Westerhold et al., 2007, 2008, 2009](#), and [Kuiper et al., 2008](#); 55.9 Ma according  
594 to [Charles et al., in press](#)). Both the PETM and the Elmo (ETM2) events are situated in  
595 the decreasing part of the strongest  $\sim 9$ -myr  $\delta^{13}\text{C}$  cycle (Cb7) with the PETM is near the  
596 inflection-point ( $\sim 56$  Ma).  
597



599 **Figure 3:**  $2\pi$ -MTM power spectra of the  $\delta^{13}\text{C}$  records (Zachos et al., 2008; Cramer et al.,  
600 2009), using the multitaper method (Thomson, 1982) as implemented in SSA-MTM  
601 Toolkit (Ghil et al., 2002). Results of noise modelling (also shown) were estimated using  
602 linear fitting and median filtering over 20% of the average Nyquist frequency range. **(a)**  
603 Zachos et al.'s (2008) compilation, dashed line: raw  $\delta^{13}\text{C}$  record linearly interpolated to a  
604  $\sim 4$ -kyr sample rate (the average sampling interval of the record is  $\sim 4.7$  kyr), solid line: 1x  
605 zero-padded  $\delta^{13}\text{C}$  used to highlight the  $\sim 8.4$ -myr peak (see also Fig. S2). **(b)** Cramer et  
606 al.'s (2009) compilation, dashed line: raw  $\delta^{13}\text{C}$  record linearly interpolated to a  $\sim 4$ -kyr  
607 sample rate (the average sampling interval of the record is  $\sim 4.7$  kyr), solid line: 1x zero-  
608 padded  $\delta^{13}\text{C}$  used to highlight the  $\sim 8.3$ -myr peak (see also Fig. S2). **(c)** Spectrum of (a)  
609 in a logarithmic format over a broader frequency band, together with the modeled red  
610 noise spectrum. **(d)** Spectrum of (b) in a logarithmic format over a broader frequency  
611 band, together with the modeled red noise spectrum.  
612



613

614 **Figure 4:**  $2\pi$ -MTM harmonic analysis of the orbital eccentricity in the La2004 (black line) and

615 La2010d (red line) astronomical models (Laskar et al., 2004, 2011a) over the last 67 Ma

616 (time interval equivalent to that in  $\delta^{13}\text{C}$  data). (a) the raw spectra displayed over

617 frequencies 0 to 0.02 cycles/kyr, and truncated amplitude axis at 0.005: only the peak

618 representing the 405 kyr eccentricity term is truncated (its full relative amplitude is

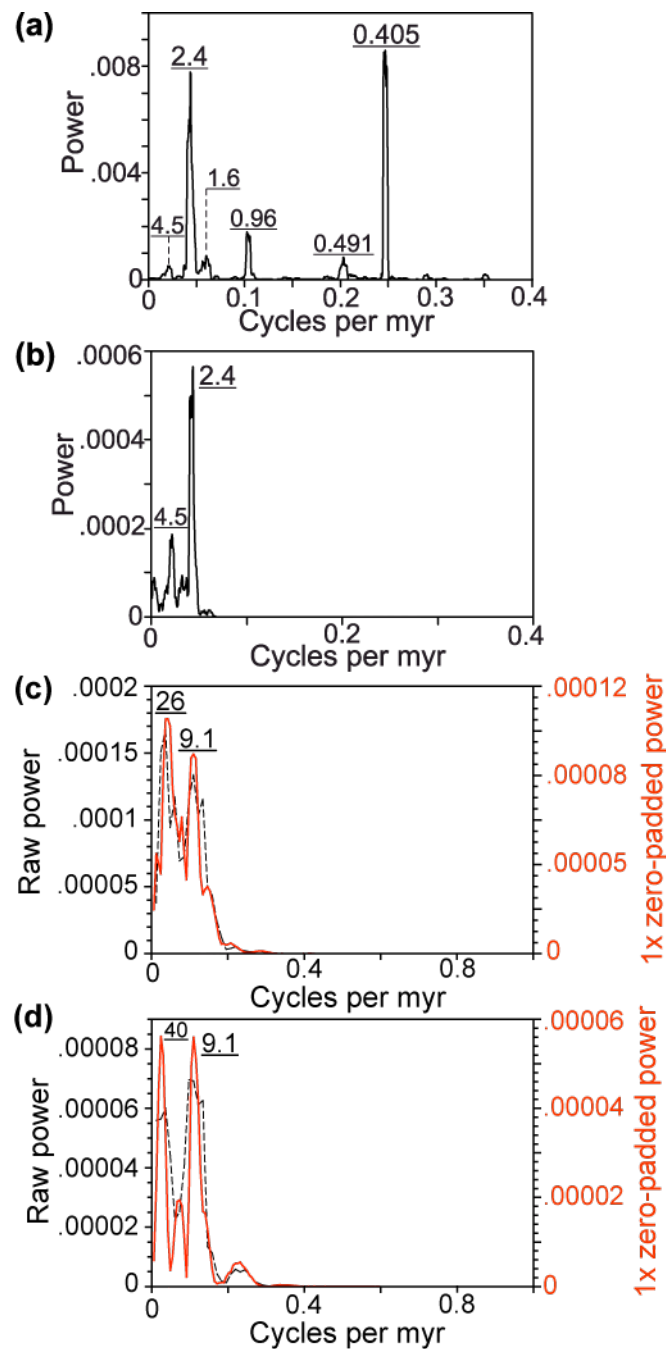
619  $\sim 0.010$ ). The truncated power axis to highlight peaks at low frequencies in the shaded

620 area. (b) a zoom of the shaded area in 'a' to well visualize low-frequency peaks, the

621 amplitude axis is also truncated at 0.003. All peaks are labelled in kyr, and the origin of

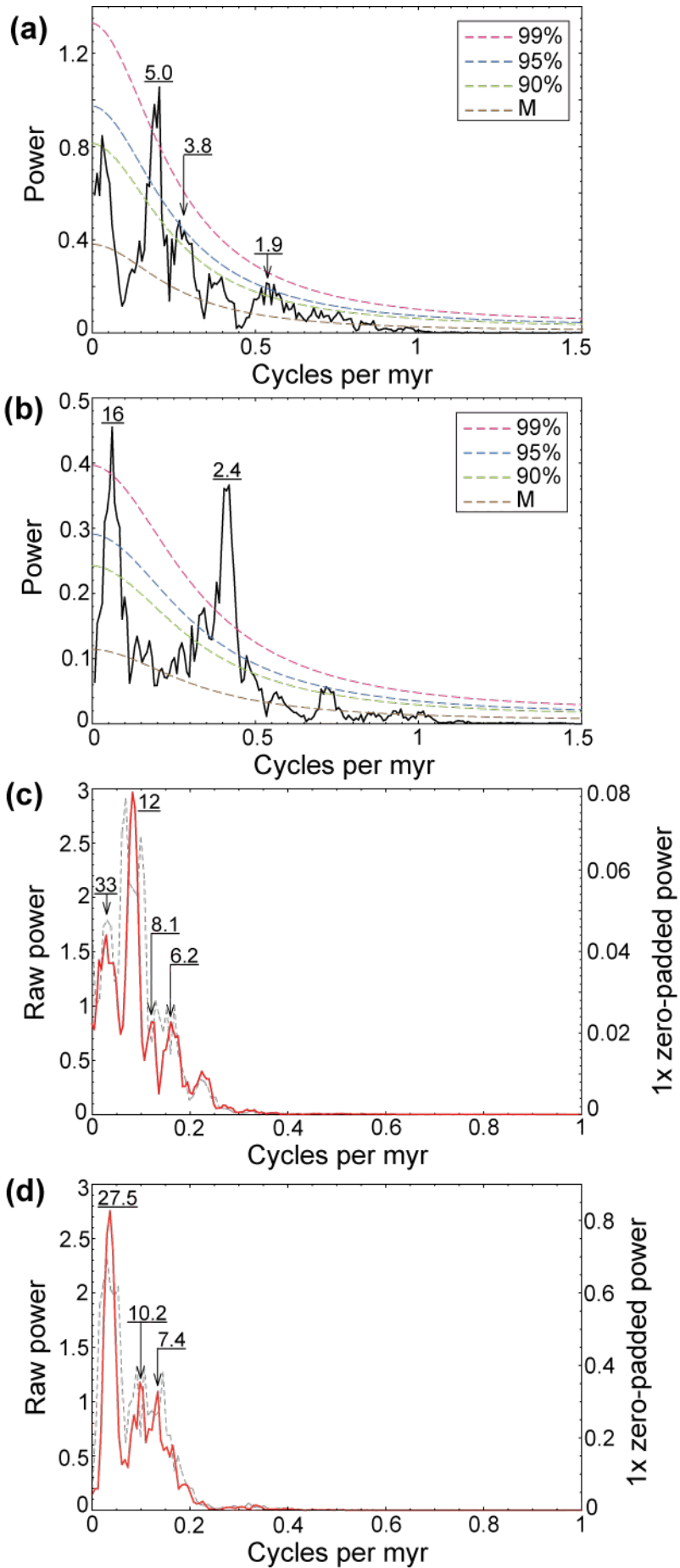
622 each eccentricity component is also shown, where  $g_1$ ,  $g_2$ ,  $g_3$ ,  $g_4$  and  $g_5$  are the secular

623 frequencies related respectively to the precession of the perihelions of Mercury, Venus,  
 624 the Earth, Mars, and Jupiter (see [Laskar et al., 2004](#) for detail). Note that only the main  
 625 peaks depicting the main eccentricity components are shown.  $\Delta f$  in 'b' equals to  
 626 0.000427 cycles/kyr, which corresponds to a period of 2342 kyr, i.e.,  $(g_4 - g_3)$  is the  
 627 result of two possible interferences of  $(g_2 - g_5)$  with  $(g_2 - g_5) - (g_4 - g_3)$ , and  $(g_2 - g_5)$   
 628 with  $(g_2 - g_5) + (g_4 - g_3)$  (see text for discussion).  
 629



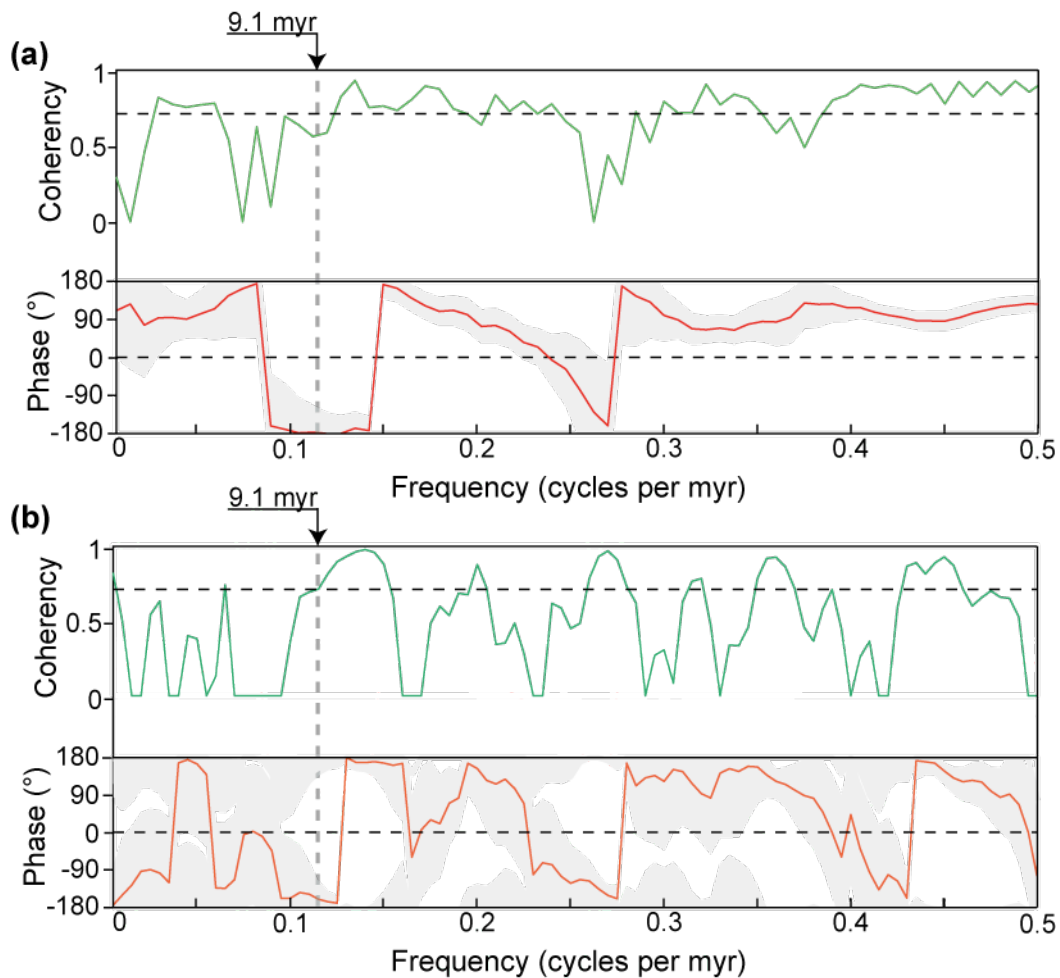
630

631 **Figure 5:**  $2\pi$ -MTM power spectra of amplitude modulation (AM) of  $\delta^{13}\text{C}$  records (Zachos et  
632 al., 2008; Cramer et al., 2009), using the multitaper method (Thomson, 1982) as  
633 implemented in SSA-MTM Toolkit (Ghil et al., 2002). Results of noise modelling (also  
634 shown) were estimated using linear fitting and median filtering over 20% of the average  
635 Nyquist frequency range. **(a)** Spectrum of the AM envelopes of the  $\sim 400$ -kyr  $\delta^{13}\text{C}$  band  
636 of Zachos et al.'s (2008) compilation (Supplementary Figure S3, solid curve 5). **(b)**  
637 Spectrum of the AM envelopes of the  $\sim 400$ -kyr  $\delta^{13}\text{C}$  band of Cramer et al.'s (2009)  
638 compilation (Supplementary Figure S3, dashed curve 5). **(c)** Spectrum of the AM  
639 envelopes of the  $\sim 2.4$ -myr  $\delta^{13}\text{C}$  band of Zachos et al.'s (2008) compilation  
640 (Supplementary Figure S3, solid curve 4), dashed line: raw AM, solid line: 1x zero-  
641 padded AM. **(d)** Spectrum of the AM envelopes of the  $\sim 2.4$ -myr  $\delta^{13}\text{C}$  band of Cramer et  
642 al.'s (2009) compilation (Supplementary Figure S3, solid curve 4), dashed line: raw AM,  
643 solid line: 1x zero-padded AM. All peaks are labelled in myr.  
644





646 **Figure 6:**  $2\pi$ -MTM power spectra of amplitude modulations (AM) of La2004 and La2010d  
647 orbital eccentricity (Laskar et al., 2004, 2011a), using the multitaper method (Thomson,  
648 1982) as implemented in SSA-MTM Toolkit (Ghil et al., 2002). (a) AM of the  $\sim$ 100-kyr  
649 La2004 eccentricity band (Fig. 1, solid curve 1). (b) AM of the  $\sim$ 400-kyr La2004  
650 eccentricity band (Fig. 1, solid curve 2). (c) Dashed line: AM of the  $\sim$ 2.4-myrr La2004  
651 eccentricity band (Fig. 1, solid curve 3), solid line: 1x zero-padded of  $\sim$ 2.4-myrr La2004  
652 eccentricity AM used to highlight the  $\sim$ 9-myrr peak. (d) Dashed line: AM of the  $\sim$ 2.4-myrr  
653 La2010d eccentricity band (Fig. 1, dashed curve 3), solid line: 1x zero-padded of  $\sim$ 2.4-  
654 myrr La2010d eccentricity AM used to highlight the  $\sim$ 9-myrr peak. All peaks are labelled in  
655 myr.  
656



657  
658 **Figure 7:** Coherency and cross-phase spectral analysis of envelopes of  $\sim$ 2.4 myr cycles of

659 eccentricity time series (Fig. 1, Curve 3) versus  $\sim 9$  myr  $\delta^{13}\text{C}$  cycles (from the raw  $\delta^{13}\text{C}$   
660 record of [Zachos et al., 2008](#) in Fig. 1, Curve 4). **(a)**  $\delta^{13}\text{C}$  versus  $\sim 2.4$  myr AM of La2004  
661 model ([Laskar et al., 2004](#)). **(b)**  $\delta^{13}\text{C}$  versus  $\sim 2.4$  myr AM of La2010d model ([Laskar et](#)  
662 [al., 2011a](#)). Note that  $\delta^{13}\text{C}$  and eccentricity are coherent at  $\sim 9$  myr cyclicity, and that  $\sim 9$   
663 myr  $\delta^{13}\text{C}$  oscillations are  $\sim 180^\circ$  out of phase with  $\sim 9$  myr eccentricity cycles. The  
664 approximate 95% confidence level for the coherence between red noise and a narrow  
665 band signal is indicated by the dashed line; the zero phase line is indicated by the  
666 dashed line, and the approximate 95% confidence interval for phase is indicated by the  
667 gray shading. Vertical dashed lines indicate the  $\sim 9.1$  myr frequency (see Figs. 5c,d). We  
668 used the cross-MTM method in the Matlab routine of Peter Huybers (e.g., [Huybers and](#)  
669 [Denton, 2008](#)).

670

671

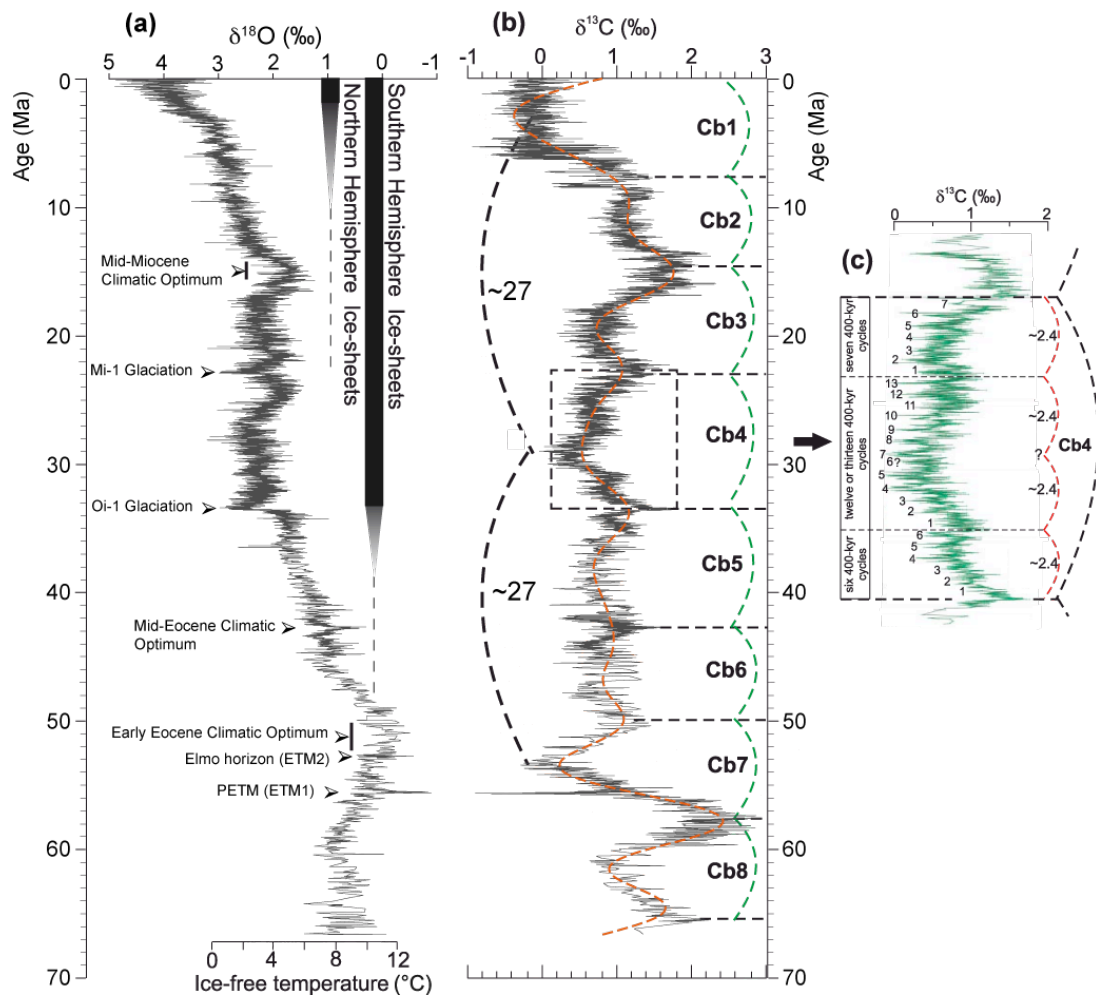
672

673 **Boulila et al.'s Supplementary Information**

674

675 **Supplementary figures**

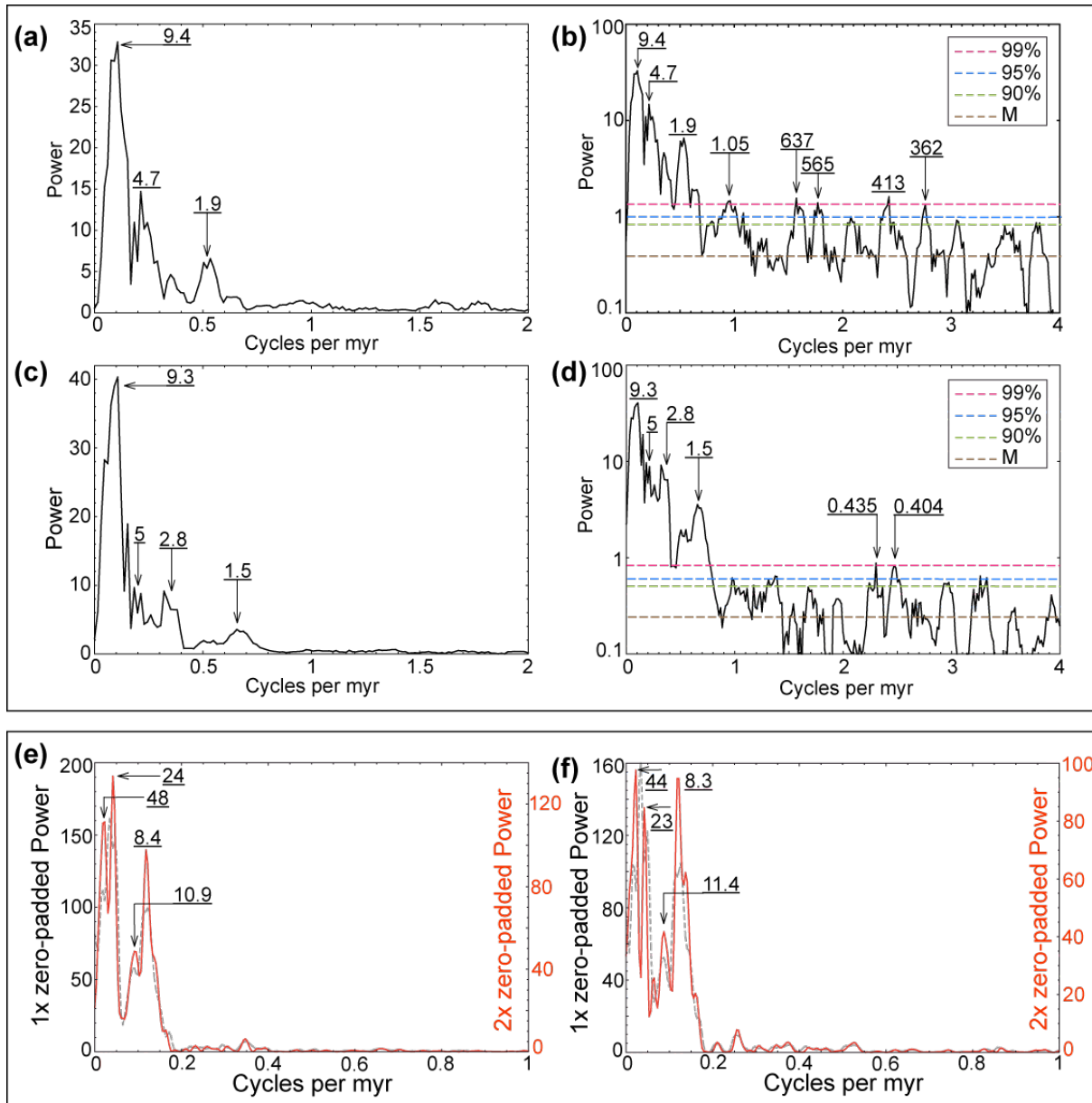
676



677

678 **Figure S1:** Global deep-sea oxygen and carbon isotope records based on data compiled  
 679 from more than 40 Deep Sea Drilling Project and Ocean Drilling Program sites (Zachos  
 680 et al., 2001, 2008). **(a)** Oxygen record, the main climatic events are also shown, ETM1  
 681 (also known as the Elmo horizon) and ETM2 (also known as PETM) represent Eocene  
 682 Thermal Maximum events, with the PETM is the Paleocene-Eocene Thermal Maximum,  
 683 the main hyperthermal event. Note that the  $\delta^{18}\text{O}$  temperature scale was computed for an  
 684 ice-free ocean ( $\sim 1.2$  ‰ standard mean ocean water, SMOW). From the early Oligocene  
 685 on, and possibly for some time before that, much of the variability in the  $\delta^{18}\text{O}$  values may  
 686 reflect volume changes in polar ice sheets. The vertical bars provide a rough estimate of  
 687 the ice volume in each hemisphere relative to the ice volume during the Last Glacial  
 688 Maximum. **(b)** Carbon isotope record, pseudo-periodic  $\sim 9$ -myr ( $\sim 7$  to  $\sim 11$  myr)  $\delta^{13}\text{C}$   
 689 cycles are shown (labelled Cb1 to Cb8). Possible  $\sim 27$ -myr  $\delta^{13}\text{C}$  cycles are also shown.

690 (c) A detailed Cb4 cycle, data from Pälke et al. (2006a) with  $\sim 4$ -kyr sampling intervals.  
 691 We identified the  $\sim 400$ -kyr and  $\sim 2.4$ -myr cycles within Cb4. The two middle  $\sim 2.4$ -myr  
 692 cycles are “amalgamated”, as are the analogous astronomical  $\sim 2.4$ -myr cycles over this  
 693 time interval (see Figs. 1 and 2a).  
 694

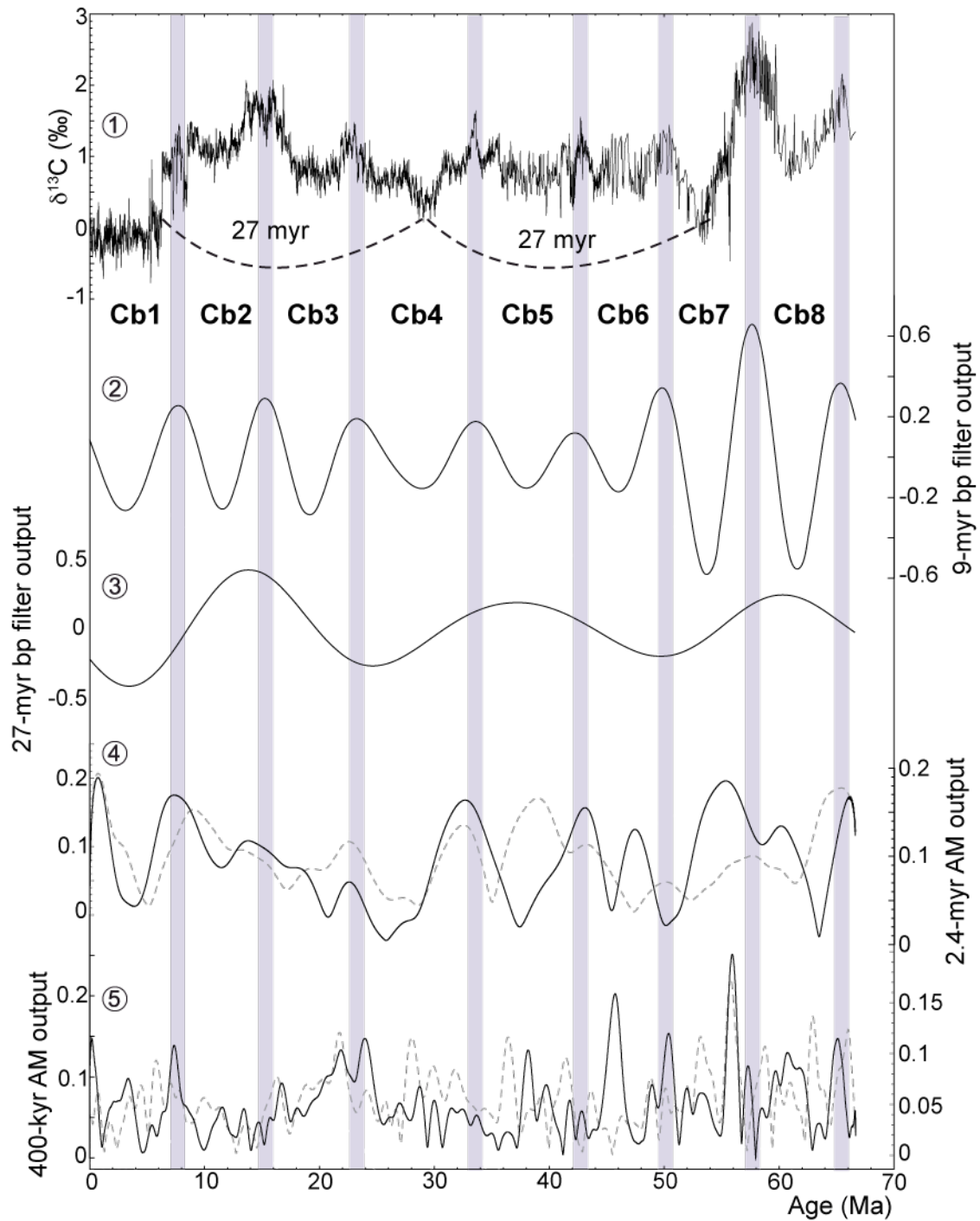


695  
 696 **Figure S2: Upper panel:**  $2\pi$ -MTM power spectra of a selected interval (16.5 to 54.5 Ma) of  
 697 Cenozoic  $\delta^{13}\text{C}$  records, after removal of a third-order polynomial fit to attenuate irregular  
 698 long-term variations due to the  $\sim 27$ - and 29-myrr oscillations (spectral peaks in main Fig.  
 699 3a,b). (a) Spectrum in a linear scale of the  $\delta^{13}\text{C}$  of Zachos et al.’s (2001, 2008)

700 compilation. **(b)** Spectrum of 'a' in a logarithmic scale over a broader frequency band,  
701 together with the modeled robust red noise spectrum. **(c)** Spectrum in a linear scale of  
702 the  $\delta^{13}\text{C}$  of Cramer et al.'s (2009) compilation. **(d)** Spectrum of 'c' in a logarithmic scale  
703 over a broader frequency band, together with the modeled robust red noise spectrum.  
704 Results of noise modelling: Curve M is the linear median-smoothed, fitted robust red  
705 noise spectrum; the upper 90%, 95% and 99% confidence limits. Note that the strongest  
706 spectral peak is centred on  $\sim 9$  myr period in both compilations (Zachos et al., 2001,  
707 2008, and Cramer et al., 2009). This supports the prominence and robustness of the 9  
708 myr  $\delta^{13}\text{C}$  oscillations (see text for discussion). **Lower panel:**  $2\pi$ -MTM power spectra of  
709 Cenozoic  $\delta^{13}\text{C}$  records of Zachos et al.'s (2008) compilation **(a)** and Cramer et al.'s  
710 (2009) compilation **(b)**. Spectra of 1x zero-padded time series (grey-dashed line as in  
711 main Figs. 3a,b) and spectra of 2x zero-padded time series (red solid line). Note that the  
712 2x zero-padding enhances the resolution of the  $\sim 8.5$  and  $\sim 25$  myr peaks. The  $\sim 46$  myr  
713 ( $48$  myr in 'e' and  $44$  myr in 'f') peak may represent a single oscillation delimited by  
714 Cb2/Cb3 and Cb7/Cb8 boundaries (Fig. S1). We used the multitaper method (Thomson,  
715 1982) as implemented in SSA-MTM Toolkit (Ghil et al., 2002). All peaks are labelled in  
716 myr.

717

718



719

720 **Figure S3:** Amplitude modulations (AM) time series of the raw  $\delta^{13}\text{C}$  records (Zachos et al.,

721 2001, 2008, Cramer et al., 2009). From top to bottom: **curve 1:**  $\delta^{13}\text{C}$  record of Zachos et

722 al. (2008) with 5-point running average, the  $\sim 9\text{-myr}$   $\delta^{13}\text{C}$  pseudo-periodic oscillations

723 (labelled Cb1 to Cb8) and the possible  $\sim 27\text{-myr}$  cycles are shown, **curve 2:**  $\sim 9\text{-myr}$

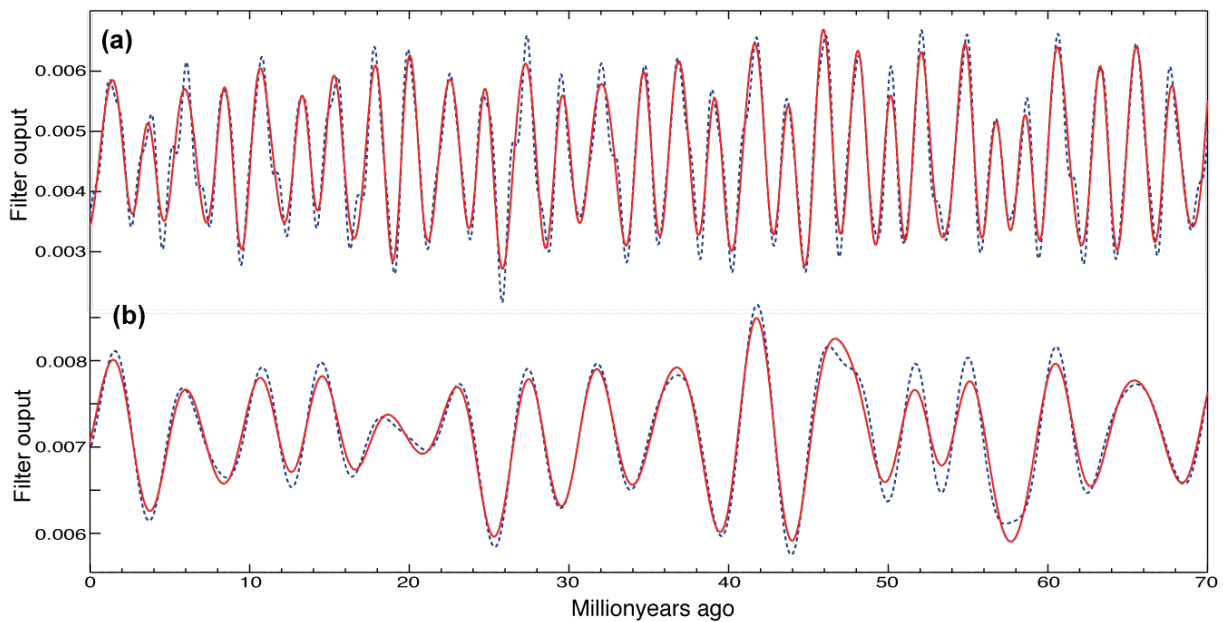
724 bandpass filter output of Zachos et al.'s (2008) raw  $\delta^{13}\text{C}$  ( $0.1265 \pm 0.0435 \text{ myr}^{-1}$  band),

725 **curve 3:**  $\sim 25\text{-myr}$  bandpass filter output of Zachos et al.'s (2008) raw  $\delta^{13}\text{C}$  ( $0.048 \pm 0.015$

726 myr<sup>-1</sup> band), **curve 4**: AM envelopes of the ~2.4-myrcentricity band ( $0.4245 \pm 0.1350$   
727 myr<sup>-1</sup> band), solid black curve: AM applied to Zachos et al.'s (2008) raw  $\delta^{13}\text{C}$ , dashed-  
728 grey curve: AM applied to Cramer et al.'s (2009) raw  $\delta^{13}\text{C}$ , **curve 5**: AM envelopes of the  
729 ~400-kyr eccentricity band ( $2.5 \pm 0.5$  myr<sup>-1</sup> band), solid black curve: AM applied to  
730 Zachos et al.'s (2008) raw  $\delta^{13}\text{C}$ , dashed-grey curve: AM applied to Cramer et al.'s (2009)  
731 raw  $\delta^{13}\text{C}$ . All band-pass filtering was performed using a Gaussian filter (Paillard et al.,  
732 1996). Before analysis,  $\delta^{13}\text{C}$  data are resampled and linearly interpolated each 0.004  
733 myr for both compilations.

734

735



736

737 **Figure S4:** Low-pass filtering of the La2004 raw eccentricity time series (Laskar et al., 2004)

738 to extract the resonant cyclicities corresponding to the argument  $\theta = 2(g_4 - g_3) - (s_4 - s_3)$

739 (Laskar, 1990; Laskar et al., 1992), where  $g_3$ ,  $g_4$  are related to the precession of the

740 perihelions of the Earth and Mars,  $s_3$ ,  $s_4$  are related to the precession of the nodes of the

741 same planets. **(a)** ~2.4 myr eccentricity cycles extracted with two different frequency-

742 cutoff bands, a moderate band (0 to 0.7 cycles/myr, solid line) and a large band (0 to 0.5

743 cycles/myr, dashed line). **(b)** ~4.5 myr eccentricity cycles extracted with two different

744 frequency-cutoff bands, a moderate band (0 to 0.28 cycles/myr, solid line) and a large  
745 band (0 to 0.33 cycles/myr, dashed line). All low-pass filtering was performed using the  
746 Taner filter (Taner, 2000).